

# Mapping the immune landscape in metastatic melanoma reveals localized cell-cell interactions correlating to immunotherapy responsiveness

**Francesca Bosisio** (✉ [francescamaria.bosisio@kuleuven.be](mailto:francescamaria.bosisio@kuleuven.be))

Translational Cell & Tissue Research, Department of Imaging and Pathology, KU Leuven, Leuven, Belgium

**Asier Antoranz**

KU Leuven

**Yannick Van Herck**

KU Leuven

**Maddalena Bolognesi**

University of Milano-Bicocca

**Seodhna Lynch**

University College Dublin

**Arman Rahman**

University College Dublin

**William Gallagher**

University College Dublin

**Veerle Boecxstaens**

KU Leuven

**Jean-Christophe Marine**

VIB-KU Leuven

**Giorgio Cattoretti**

Universita' degli Studi Milano-Bicocca

**Joost van den Oord**

KU Leuven

**Frederik De Smet**

Laboratory for Precision Cancer Medicine, Translational Cell and Tissue Research, Department of Imaging & Pathology, KU Leuven <https://orcid.org/0000-0002-6669-3335>

**Oliver Bechter**

KU Leuven

**Keywords:**

**Posted Date:** February 9th, 2022

**DOI:** <https://doi.org/10.21203/rs.3.rs-1236531/v1>

**License:**   This work is licensed under a Creative Commons Attribution 4.0 International License.

[Read Full License](#)

---

1 **Mapping the immune landscape in metastatic**  
2 **melanoma reveals localized cell-cell**  
3 **interactions correlating to immunotherapy**  
4 **responsiveness**

5  
6 **Abstract**

7 While immune checkpoint-based immunotherapy (ICI) shows spectacular clinical results in  
8 cancer patients, only a subset of these respond favorably to such treatment. Response to  
9 ICI is dictated by the integration of complex networks of cellular interactions between malignant  
10 and non-malignant cells. Although new insights into the mechanisms that modulate the pivotal  
11 anti-tumoral activity of cytotoxic T-cells (Tcy) have recently been gained, much of what we  
12 have learned is based on single-cell analyses of dissociated tumor samples; therefore, we lack  
13 critical information about the spatial distribution of the relevant cell types. Here, we used  
14 multiplexed immunohistochemistry to spatially characterize the immune landscape of  
15 metastatic melanoma from responders vs non-responders to ICI. By creating such high-  
16 dimensional pathology maps, we show that Tcy gradually evolve towards an exhausted  
17 phenotype as they approach and infiltrate the tumor. Moreover, our analysis revealed a key  
18 cellular interaction network that functionally links Tcy and PD-L1+ macrophages. Critically,  
19 mapping the respective spatial distribution of these two cell populations predict response to  
20 anti-PD-1 immunotherapy with high confidence. We conclude that baseline measurements of  
21 the spatial context should be integrated in the design of predictive biomarkers to identify  
22 patients likely to benefit from ICI.

## 23 **Introduction**

24 Treatment of malignant melanoma has been revolutionized by the introduction of anti-  
25 PD-1-based immune checkpoint inhibitors (ICI)<sup>1-4</sup>. Despite having improved overall survival  
26 and providing durable response, the outcome of immune checkpoint blockade is very variable,  
27 with most stage IV patients still succumbing to the disease<sup>1-4</sup>. Nonetheless, ICI therapy has  
28 become a standard of care in melanoma and many other solid cancers.

29 The widespread use of immunotherapy, the variable results obtained in different tumor  
30 types, the considerable and sometimes irreversible toxicity in roughly 20% of the patients and  
31 the treatment-associated costs have made the search for predictive biomarkers a pressing  
32 issue more than ever before in oncology. Consequently, researchers were prompted to  
33 investigate the tumor microenvironment (TME) more thoroughly. As a result, a plethora of  
34 different factors correlating with immunotherapy outcome have emerged, including both tumor  
35 intrinsic (e.g. tumor mutational burden<sup>5-7</sup>, aberrant tumor MHC-II expression<sup>8</sup> and tumor-  
36 related signatures<sup>6,9-12</sup>) and host intrinsic (e.g. defects in antigen presentation machinery<sup>13,14</sup>,  
37 tumor-infiltrating lymphocytes (TILs)<sup>15,16</sup>, tumor-infiltrating B cells<sup>17-19</sup> and T-cell gene  
38 expression signatures<sup>20-24</sup>) factors. However, none of these factors have thus far been broadly  
39 implemented in the clinic, partly due to a low predictive value when used as a single marker.  
40 In addition, we are still lacking a profound understanding of the mechanism(s) that make anti-  
41 PD-1 based therapy successful in one patient and unsuccessful in another. Similarly to how  
42 next-generation sequencing has made it possible to match mutational profiles to specific  
43 targeted therapies (i.e., BRAF- and MEK inhibitors)<sup>25-28</sup>, unraveling and improving response to  
44 immunotherapy will require an accurate spatial description of the inflammatory landscape  
45 within the tumor area and the specific understanding of the contribution of each factor of the  
46 complex immune response machinery.

47 Recently, the pre-existent CD8+ T-cell effector response resulting from chronic tumor  
48 antigen exposure and the dynamics following checkpoint blockade has been elucidated more  
49 thoroughly. A subset of T<sub>cy</sub> that display stem-like properties and that promote tumor control in  
50 response to checkpoint blockade immunotherapy has been identified<sup>29-33</sup>. These so-called  
51 progenitor exhausted T-cells are responsible for the proliferative T-cell burst after  
52 administration of anti PD-1<sup>31,34-36</sup>. There is substantial evidence that response to checkpoint  
53 blockade is not due to reversal of a T-cell exhaustion phenotype but rather depends on  
54 proliferation of this stem-like subset of T-cells. After eliciting a cytotoxic effect these cells can  
55 further differentiate into 'terminally exhausted' T<sub>cy</sub>. Data supporting this model are mostly  
56 generated by methods based on tissue dissociation followed by single cell analysis, such as  
57 single-cell RNA sequencing (scRNA-seq) or mass cytometry. Obviously, these techniques  
58 exclude spatial information, thereby precluding the analysis of crucial cell-cell interactions  
59 within the context of the original tissue. To partially overcome this, algorithms for analyzing  
60 scRNA-seq data have been developed to screen for ligand-receptor interactions across all cell  
61 types present in a tumor microenvironment (CellPhoneDB<sup>37</sup>/ NicheNet<sup>38</sup>). These predictive  
62 methods are based on prior knowledge of signaling and gene regulatory networks, and while  
63 very interesting at producing novel hypotheses, these still require validation at the tissue level.  
64 In addition, computational methods to analyze dissociated cells are devoid of visual control  
65 and thus bear the risk for inaccurate results. Finally, RNA-based findings may also not translate  
66 to the proteomic level, thereby leaving the final executors of most biological interactions  
67 unidentified. Considering that immune reactions rely on multiple cell-cell interactions, a study  
68 of the mechanism of an immune response upon anti-PD-1 treatment should also include spatial  
69 information. Knowing the spatial distribution of the different inflammatory cell subtypes could

70 further fuel our understanding on how immunotherapy works while revealing novel potential  
71 therapeutic mechanisms or novel targets with translational clinical utility.

72 In this study, we used high-dimensional multiplexed immunohistochemistry according  
73 to the MILAN (Multiple Iterative Labeling by Antibody Neodeposition)<sup>39</sup> method through which  
74 we visualized 77 immune and tumor-related markers at single-cell resolution. As such, we  
75 characterized the cellular composition, architecture, and sociology of the immune landscape  
76 in metastatic melanoma, which allowed us to create a detailed, high-dimensional pathology  
77 map of Tcy, in which the detailed phenotype of the different Tcy subsets and their exact  
78 location in clinical biopsies is identified. This analysis did not only confirm previous findings at  
79 the proteomic level, but it also allowed us to visualize and study the sociology between the  
80 cellular subsets within their native tissue context. By subsequently applying novel spatial  
81 analysis approaches, we were able to construct a spatial trajectory within the tumor in parallel  
82 to and corresponding with a pseudotime differentiation trajectory of Tcy, showing that Tcy  
83 gradually evolved towards more exhausted phenotypes as they approached and infiltrated the  
84 tumor. Finally, we studied the interaction between Tcy and their local immune  
85 microenvironment, thereby revealing a role for interactions between Tcy and PD-L1+  
86 macrophages in the distinction between responders (RESP) and non-responders (NRESP) to  
87 anti-PD-1 immunotherapy, insights that outcompete earlier measurements that did not take a  
88 spatial component into account.

89

## 90 **Material and Methods**

91

### 92 **Clinical data**

93 A cohort of 16 pre-treatment, frozen melanoma metastasis lesions from 14 different  
94 patients was selected for Nanostring Gene Expression Analysis. All patients were treated with  
95 anti-PD-1 monotherapy (nivolumab or pembrolizumab) after the biopsy was taken. Only  
96 biopsies taken < 365 days before the start of checkpoint inhibition therapy were included.  
97 Furthermore, only patients with measurable disease were selected, hence enabling tumor  
98 response assessment according to RECIST 1.1<sup>40</sup>. Patients were classified according to the  
99 best objective response (BOR) to immunotherapy during their time of follow up, as defined by  
100 RECIST 1.1<sup>40</sup>. Complete response (CR) and partial response (PR) were classified as RESP,  
101 progressive disease (PD) or stable disease (SD) as NRESP. According to these criteria, 7  
102 patients could be classified as RESP (8 samples) and 7 patients as NRESP (8 samples).

103 A cohort of 24 pre-treatment, formalin-fixed, paraffin embedded (FFPE) melanoma  
104 metastasis samples from 21 patients from the University Hospital of Leuven was collected. Out  
105 of these samples, 12 were also included in the Nanostring analysis. Primary lesions were  
106 excluded. Pathologists selected the most representative areas of the tumors for tissue  
107 microarray (TMA) construction. For each metastasis, one to five representative cores/regions  
108 of interest were sampled having at least a size of 2 mm in diameter. The number of samples  
109 taken was determined by the specimen and the morphological heterogeneity of both the  
110 melanoma and the inflammatory infiltrate. Therefore, a smaller number of cores were taken  
111 from small and homogeneous samples whereas a larger number was taken from large but  
112 heterogeneous specimens. In total, 70 cores/regions of interest were selected for analysis.  
113 The TMAs were constructed with the TMA Grand Master (3DHistech Ltd., Budapest, Hungary).  
114 A subset of patients included were treated with anti-PD-1 monotherapy (nivolumab or  
115 pembrolizumab) after the biopsy was taken. Biopsies taken  $\geq$  365 days before the start of  
116 checkpoint inhibition therapy were excluded. Following similar response stratification criteria  
117 used in the Nanostring patient cohort, 7 out of 21 patients could be classified as RESP (7

118 samples) and 8 out of 21 patients as NRESP (9 samples). For 6 patients (8 samples) response  
119 assessment was not possible due to several reasons (e.g. no subsequent therapy with anti-  
120 PD-1 treatment, sample too old according to our cut-off of 365 days). In order to exclude noise  
121 in the downstream analysis regarding factors associated with response, these 6 patients were  
122 included for the evaluation of the immune landscape but were excluded from the correlation  
123 analysis with response. An overview of the samples/patients included in this study is provided  
124 in Suppl. Table 1. This project was approved by the Ethical Commission of the University  
125 Hospital of Leuven.

126

### 127 **Nanostring Gene Expression Analysis**

128 The frozen material was analyzed using the PanCancer Immune Profiling Panel of the  
129 nCounter technology from Nanostring. Transcriptomic counts were log<sub>2</sub> transformed.  
130 Differential gene expression of RESP patients versus NRESP patients was calculated using  
131 the limma R package<sup>41</sup>. Enriched pathways were identified using the piano R package<sup>42</sup>. From  
132 the different gene set analysis methods included in the Piano pipeline we selected the following  
133 10 using the gene-level-statistic defined in parenthesis: fisher (p-value), stouffer (p-value),  
134 reporter (p-value), page (t-value), tailStrength (p-value), gsea (t-value), mean (logFC), median  
135 (logFC), sum (logFC), and maxmean (t-value). P-values from the different gsa methods were  
136 summarized by calculating the median ranking of the individual methods and then mapping  
137 the corresponding p-value for the obtained rank. For the gene sets, the Molecular Signatures  
138 Database (MSigDB)<sup>43</sup>, curated pathways (c2), canonical pathways (cp), version 7.2 was used.  
139 Insights in general sample cytometry were gained using CibersortX<sup>44</sup> with the LM22 signature  
140 matrix. Insights in Tcy specific cell populations cytometry were obtained by first creating a  
141 custom signature matrix using the data and defined cell states by Sade-Feldman and  
142 colleagues<sup>29</sup> and CibersortX's "Create Signature Matrix" module. Tcy proportions were then  
143 estimated using the "Impute Cell Fractions" module.

144

### 145 **MILAN multiplex staining and image acquisition**

146 Multiplex immunofluorescent staining was performed according to the previously  
147 published MILAN protocol<sup>39</sup>. The antibody panel for MILAN was designed to allow a phenotypic  
148 identification of the most abundant cell types based on the results from the Nanostring analysis  
149 and the scRNA-seq data from others<sup>29,45</sup>, including a more in-depth functional characterization  
150 of T-cells based on literature review. An overview of the panel with the 77 markers included  
151 and the specifications about the primary and secondary antibodies can be found in Suppl.  
152 Table 2. Immunofluorescence images were scanned using the NanoZoomer S60 Digital slide  
153 scanner (Hamamatsu, Japan) at 20X objective with resolution of 0.45 micron/pixel. The  
154 hematoxylin and eosin slides were digitized using the Axio scan.Z1 slidescanner (Zeiss,  
155 Germany) in brightfield modus using a 20X objective with resolution of 0.22 micron/pixel.

156

### 157 **Image Quality control and Analysis**

158 The stainings were visually evaluated for quality by digital image experts and  
159 experienced pathologists (FMB, GC, and YVH, triple blinded). Multiple approaches were taken  
160 to ensure the quality of the single-cell data. On the image level, the cross-cycle image  
161 registration and tissue integrity were reviewed; regions that were poorly registered or contained  
162 severely deformed tissues and artifacts were identified, and cells inside those regions were  
163 excluded. Antibodies that gave low confidence staining patterns by visual evaluation were  
164 excluded from the analyses. Image analysis was performed in Fiji/ImageJ following a  
165 procedure previously described<sup>46</sup>. Briefly, DAPI images from consecutive rounds were aligned

166 (registered) using the Turboreg and MultiStackReg plugins from Fiji/ImageJ (version 1.51 u).  
167 The coordinates of the registration were saved as Landmarks and applied to the rest of the  
168 channels. Tissue autofluorescence was subtracted from an acquired image in a dedicated  
169 channel, for FITC, TRITC and Pacific Orange. The TMA was segmented into tissue cores using  
170 a custom macro. Core segmentation was followed by watershed cell segmentation and single-  
171 cell measurements which were performed using the EImage R package<sup>47</sup>. For every cell, the  
172 extracted features included: X/Y coordinates, nuclear size, and Mean Fluorescence Intensity  
173 (MFI) for all the measured markers.

174

## 175 **Phenotypic Identification**

176 MFI values were normalized within each core to Z-scores as recommended in Caicedo  
177 et al<sup>48</sup>. Z-scores were trimmed in the [0, 5] range to avoid a strong influence of any possible  
178 outliers in downstream analyses. Single cells were mapped to known cell phenotypes using  
179 three different clustering methods: PhenoGraph<sup>49</sup>, FlowSom<sup>50</sup>, and KMeans as implemented  
180 in the Rphenograph, FlowSOM, and stats R packages. While FlowSom and KMeans require  
181 the number of clusters as input, PhenoGraph can be executed by defining exclusively the  
182 number of nearest neighbors to calculate the Jaccard coefficient<sup>49</sup> which was set to 12.  
183 PhenoGraph groups the input cells into a number of numeric clusters (1,2,...,n) with similar  
184 expression profiles. The number of clusters identified by PhenoGraph was then passed as an  
185 argument for FlowSom and KMeans.

186 Clustering was performed exclusively in a subset of the identified cells (50,000)  
187 selected by stratified proportional random sampling and using only the markers defined as  
188 phenotypic (Suppl. Table 2). The stratification was performed by selecting a number of cells in  
189 each sample equal to the relative proportion of the number of cells in that sample in the entire  
190 dataset. That is:

191 
$$S_i = S \cdot \frac{N_i}{M}, \text{ where } M = \sum_{i=1}^P (N_i)$$

192 where  $S_i$  is the number of cells to be sampled for the  $i$ -th sample,  $S$  is the total number of cells  
193 to be sampled (here 50,000),  $N_i$  is the number of cells in the  $i$ -th sample, and  $M$  is the total  
194 number of cells in the dataset (sum of all samples,  $P$ ).

195 For each clustering method, clusters were mapped to known cell phenotypes following  
196 manual annotation from domain experts (FMB, YVH, double blinded). If two or more clustering  
197 methods agreed on the assigned phenotype, the cell was annotated as such. If all three  
198 clustering methods disagreed on the assigned phenotype, the cell was annotated as “not  
199 otherwise specified, NOS”. For each phenotype, a fingerprint summarizing the average  
200 expression of each marker for all the cells of the given phenotype was constructed. These  
201 fingerprints were used to predict the phenotype of all the cells included in the dataset (minimum  
202 of Euclidean distance).

203

## 204 ***In-silico* tissue microdissection**

205 We further dissected the analyzed samples into tumor areas (TA), tumor-stroma  
206 interface (TSI), and non-tumor areas (NTA) (Suppl. Fig. 1). To that end, tissues were  
207 fragmented into 50x50 pixel tiles (22.5 sq. micrometers). Tiles with at least 1 cell identified as  
208 melanoma were initially defined as TA. To reduce the impact of potential outliers, a median  
209 filter was applied to the obtained tumor masks. The tumor edge was defined as the overlap  
210 between the dilated tumor mask (box kernel of 5px of diameter), a dilated non-tumor mask  
211 (complementary of the tumor mask, box kernel of 5px of diameter), and the complement of a

212 dilated mask positive for the areas without tissue (i.e., outside mask, box kernel of 5 tiles,  
213 251px of diameter). The complement of the outside mask was used to remove the tumor edge  
214 in areas close to the contour of the tissue as predictions around the contour are often  
215 unreliable<sup>51</sup>. The TSI was defined at 150 pixels (67.5 micrometers) symmetrically towards and  
216 away from the tumor edge (that is, the border between the tumor and the stroma). This was  
217 calculated by dilating the tumor-edge with a box kernel of 301 pixels in diameter. The rest of  
218 the tissue was defined as NTA. We evaluated the immune populations present in each  
219 microdissected area by comparing the proportion of each identified immune phenotype relative  
220 to the total immune population (pairwise, Wilcoxon test). Adjustment for multiple comparisons  
221 was performed using the false-discovery rate (FDR) method.

222

### 223 **High-dimensional proteomic profiling of Tcy**

224 Tcy were further profiled based on the expression of the following 10 markers:  
225 CD137/4-1BB, CD69, CD7, CD74, CXCR5, granzyme B (GrB), PD-1, TCF7, TIM-3, and VISTA  
226 ('Tcy panel', Suppl. Table 2). A subset of all the identified Tcy (stratified sampling, 6,000 cells)  
227 was clustered using KMeans and manually annotated by domain experts (FMB, YVH).  
228 Fingerprints were used to calculate the status of all the Tcy included in the dataset (minimum  
229 of Euclidean distance). For all the identified subtypes, we looked for enrichment in the different  
230 *in-silico* microdissected areas by checking the proportion relative to all the immune cells of  
231 each identified subtype between the areas (pairwise, Wilcoxon test). Adjustment for multiple  
232 comparisons was performed using the false-discovery rate (FDR) method.

233 Additionally, we assigned an activation score to each Tcy based on a previously  
234 published model which integrates the expression of TIM-3 and LAG3 as exhaustion markers  
235 and CD69 and OX40 as activation markers into a single score in the [-1, 1] range<sup>46</sup>. We looked  
236 for differences in Tcy activation in the different *in-silico* microdissected areas (generally for all  
237 Tcy and specifically for each identified subtype) by applying t-tests (two-tails, FDR corrected)  
238 on the average activation of each core. We also investigated how the distance to the tumor  
239 edge affected Tcy activation. To that end, we calculated the Euclidean distance of each Tcy to  
240 the closest point in the tumor edge, grouped the Tcy in bins of 10 micrometers, and calculated  
241 the average activation score of all the Tcy in each bin. Distances towards the tumor were  
242 defined negative while distances away from the tumor were defined positive. To avoid patient-  
243 to-patient variability, we previously normalized the activation of the Tcy by taking z-scores in  
244 each core. We fitted a cubic smoothing spline function to the generated curve, calculated its  
245 first-order derivative, and looked for the point in the X-axis (distance to the tumor edge) where  
246 the Y-axis (derivative of Tcy activation) was maximum, that is, the point where the Tcy  
247 activation score changes the most.

248

### 249 **Spatial dynamics of Tcy differentiation**

250 Next, we assessed the spatial evolution of Tcy subtypes based on their distance to the  
251 tumor edge. To that end, first, we calculated the probability ( $P_{i,j}$ ) of each Tcy ( $i$ ) belonging to  
252 any of the categories manually annotated ( $j$ ) as follows:

$$253 \quad P_{i,j} = \frac{1}{M_{i,j}} \cdot w_i$$

254 where  $M_{i,j}$  is the euclidean distance of the expression of  $Tcy_i$  to the fingerprint of the subtype  
255  $j$ , and  $w_i$  is the sum of the inverse distances of  $Tcy_i$  for all the subtypes, that is:

$$256 \quad w_i = \sum_{j=1}^N \frac{1}{M_{i,j}}$$

257 where N is the total number of identified subtypes. Essentially,  $w_i$  guarantees that:

258 
$$\sum_{j=1}^N P_{i,j} = 1$$

259 Then, we calculated the distance of each Tcy to the tumor edge. Distances towards  
260 the tumor were defined negative while distances away from the tumor were defined positive.  
261 Continuous distance values were grouped in bins of 10 micrometers. For each bin, we  
262 calculated the probability of belonging to each subtype by averaging the probabilities of all the  
263 Tcy included in the bin.

264

### 265 **Spatial lineage analysis**

266 We correlated the spatial distance of Tcy to the tumor edge with a pseudotime value  
267 obtained after applying slingshot<sup>52</sup>. To that end, PD-1, GrB, TIM-3, CD69, TCF7, and Ki67  
268 expression values were normalized (z-scores) in a number of preselected Tcy subtypes. After  
269 normalization, a subset of the data (500 cells per Tcy subtype) was randomly sampled. Then,  
270 diffusion maps as implemented in the destiny R package<sup>53</sup> were used to dimensionally reduce  
271 the data to 3 components. The rest of the dataset was projected on the reduced space using  
272 the dm\_predict function. Lineages and trajectories were calculated using the getLineages and  
273 getCurves functions from the slingshot R package<sup>52</sup>. The obtained pseudotime score was  
274 normalized in the [0-1] range. We correlated the density of Tcy subtypes, their spatial location,  
275 and the expression of each of the included markers in this analysis with the obtained  
276 normalized pseudotime score.

277

### 278 **Data reporting**

279 All samples were stained simultaneously. Image-acquisition order was distributed  
280 spatially and independently of patient or tumor replicates. Image acquisition, single-cell  
281 quantification and clustering were blinded to patient identifiers and clinical metadata. No  
282 statistical methods were used to predetermine sample size.

## 283 **Results**

### 284 **1. Nanostring Gene Expression Analysis**

285 As a first attempt to explore major differences between RESP and NRESP to anti-PD-  
286 1 therapy, we performed bulk transcriptomic analysis using the PanCancer Immune Profiling  
287 Panel of the Nanostring nCounter technology on the frozen material available (whole tumoral  
288 nodules) from 16 metastatic melanoma samples (8 RESP, 8 NRESP, clinical data can be found  
289 in Suppl. Table 1). In total, 10 out of 784 genes included in the gene panel were differentially  
290 expressed (Suppl. Table 4). CD4, DDX58, MAP2K4, and KLRF1 were overexpressed in RESP  
291 patients, while HSD11B1, MFGE8, IGF1R, APP, TNFRSF11B (OPG), and A2M were  
292 underexpressed (Suppl. Fig. 2A). Some of these genes are already known for their role in the  
293 tumoral immune response and in some cases, in response to immunotherapy. DDX58 and  
294 MAP2K4 have been associated with response to anti-CTLA and MEK-inhibition respectively<sup>54-  
295 56</sup>, whereas KLRF1 is associated with natural killer cell infiltration, T-cell exhaustion and  
296 reduced TNF/IFN-gamma production<sup>57</sup>. On the other hand, several of the underexpressed  
297 genes are known to be associated with specific remodeling of the tumoral microenvironment,  
298 for instance the production of OPG or alpha-2 macroglobuline (A2M) with potential cytokine  
299 scavenger properties<sup>58-60</sup>, M2 polarization of tumor-associated macrophages via IGF-1 and  
300 MFG-E8<sup>61,62</sup>, or the inhibition of proliferation among tumour-specific CD8+ T-cells by means of  
301 increased local cortisol with the induction of HSD11B1<sup>63</sup>. Subsequently, performing gene set  
302 enrichment/pathway analysis, we could observe significant differences between RESP and  
303 NRESP (Suppl. Table 5). We observed in RESP an upregulation of B- and T-cell related  
304 pathways and of pathways involved in the adaptive immune system like B lymphocyte  
305 pathway, CSK pathway, TCR signaling pathway, TCRA pathway, among others (Suppl. Fig.  
306 2B). When evaluating the cell fractions obtained after using CibersortX, we did not find  
307 significant cell differences in general cell composition (LM22) or in Tcy subtypes (Suppl. Fig.  
308 2C-D). We used these results to assemble a specific antibody panel for the subsequent *in situ*  
309 single cell analysis, focusing on the lymphocytic, macrophagic and antigen presenting cells  
310 compartment.

311

### 312 **2. Immune landscape & *in-silico* microdissection**

313 Using MILAN (see methods), we were able to identify 1,426,617 cells (average of  
314 67,934.14 cells per patient, standard deviation of 52,588.52; range of 7,316-247,806)  
315 containing information on nuclear size, X/Y coordinates, and expression (MFI) for each of the  
316 77 markers included in the analysis (Suppl. Table 2). Applying unsupervised consensus  
317 clustering (see methods, phenotypic identification) by using a panel of 37 selected phenotypic  
318 markers, we identified 67 clusters that were manually annotated to 18 cell phenotypes, each  
319 corresponding to a specific protein signature/fingerprint, characterized by the following main  
320 markers (Fig. 1A-B, Suppl. Fig. 3C-F): B-cells ("BC"; CD20, CD79a and PAX5), plasma cells  
321 ("PC"; CD138 and PRDM1), classical dendritic cells type 1 ("cDC1"; CD141 and IRF8),  
322 classical dendritic cells type 2 ("cDC2"; CD1c), follicular dendritic cells ("fDC"; CD23 and  
323 CD21), plasmacytoid dendritic cells ("pDC"; CD303), cytotoxic T-cells ("Tcy"; CD3 and CD8),  
324 T helper cells ("Th"; CD3 and CD4), regulatory T-cells ("Treg"; CD3, CD4 and FOXP3), blood  
325 vessels ("BV"; CD31 and CD34), high endothelial venules ("HEV"; PNA<sup>d</sup>), lymphatic vessels  
326 ("LV"; Podoplanin), epithelial cells (CK), M1-like macrophages (CD68, CD64 and LYZ), M2-  
327 like Macrophages (CD68, CD64 and CD163), and melanoma (S100B and Melan-A). Clusters  
328 with the expression of several markers without an obvious phenotypic profile were annotated  
329 as "not otherwise specified, NOS". Clusters with no expression of any phenotypic marker were  
330 annotated as "blank". From the 49,998 cells included in the clustering (2 cells less than the

331 50,000 due to rounding effects on the stratification), 24,767 (49.54%) showed agreement in  
332 the assigned phenotype between all 3 included clustering methods, 21,685 (43.37%) showed  
333 agreement between 2 clustering methods, and 3,546 (7.09%) showed an inconsistent  
334 phenotype assignment. Cells with an inconsistent labelling between the different clustering  
335 methods were also labelled as “NOS” (Suppl. Fig. 3G-I). Based on the predicted phenotypes  
336 and the X/Y coordinates of each individual cell, the tissue was digitally reconstructed,  
337 resembling the morphology of the corresponding hematoxylin & eosin-staining of a previous  
338 section, but showing the phenotypic identity of each cell type (Fig. 1D-F). General sample  
339 composition is summarized in Suppl. Table 3. We did not find significant differences in general  
340 cell composition between RESP and NRESP (Wilcoxon rank-sum test, two tails).

341 Next, using the phenotypical identity of each cell within the digitally reconstructed  
342 tissue, we further *in-silico* microdissected the tissue, separating tumor area (TA), tumor-stroma  
343 interface (TSI), and non-tumor areas (NTA) (Fig. 1G, Suppl. Fig. 4A). Overall, 51% of the areas  
344 were labelled as tumor (inter-patient SD = 17.44%, range 13.24-75.28%), 24.6% as TSI (SD  
345 = 6.97%, range 15.07-39.88%), and 24.4% as non-tumor (SD = 14.4%, range 5.29-59.32%),  
346 with a large interpatient variability (Suppl. Fig. 4B). Based on the different areas, the global cell  
347 composition was redefined into an area-specific cell composition. In the TSI 29.54% of the  
348 cells were melanoma cells (compared to 76.39% in the TA). On the contrary, in the TA,  
349 approximately 23.61% of the cells were identified as non-melanoma cells, mainly 12.77% of  
350 cells corresponding to the infiltrating immune cells: M1-like macrophages (3.13%), M2-like  
351 macrophages (2.56%), Th (1.21%), pDC (1.06%), Tcy (1.02%), cDC1 (0.98%), BC (0.81%),  
352 PC (0.75%), cDC2 (0.62%), Treg (0.5%), and fDC (0.17%). The remaining cells in the TA  
353 corresponded to BV (1.76%), LV (0.9%), NOS (0.82%), HEV (0.61%), epithelial cells (0.21%),  
354 and blanks (6.53%). Subsequently, the relative proportion of the various immune cells was  
355 compared between the different areas (Fig. 1C, Suppl. Fig. 4C, Suppl. Table 3). As expected,  
356 most lymphocytes (BC, Th and Treg) were significantly enriched in the NTA compared to the  
357 TA with an intermediate level in the TSI. Tcy on the contrary peaked within the TSI with a  
358 significant enrichment compared to the TA but no significant enrichment compared to the NTA.  
359 Remarkably, both M1-like and M2-like macrophages were significantly enriched in the TA  
360 compared to the TSI and NTA. In fact, macrophages represented the most abundant immune  
361 cell type within the TA (3.13% M1-like and 2.56% M2-like) in our patient cohort. Finally, when  
362 comparing the immune composition of RESP versus NRESP, no significant differences could  
363 be found, both overall (Suppl. Fig. 5A) as well as in the different microdissected areas (Suppl.  
364 Fig. 5B).

365

### 366 3. High-dimensional proteomic profiling of cytotoxic T-cells

367 Based on the pivotal role of Tcy in mounting an anti-tumor response, we further focused  
368 our analysis on Tcy. To gain deeper insights into the different Tcy subsets present *in situ* at  
369 the proteomic level, we performed a second level of clustering using the expression of 10  
370 markers that were not included in the first level clustering, now exclusively focusing on the  
371 previously identified Tcy. KMeans identified 34 clusters that after manual annotation were  
372 mapped to 9 Tcy subtypes, each with a specific protein signature/fingerprint (Fig. 2A-C, Suppl.  
373 Fig. 6A-B). Cluster Tcy01 represents the largest group of Tcy (37.60% of Tcy), yet this subset  
374 does not express any of the included markers. As such, the biological relevance of these cells  
375 cannot be specified further. Tcy02 (1.93%) is characterized by isolated high expression of  
376 CXCR5, corresponding to a distinct CXCR5+ Tcy subset within the B cell follicle and germinal  
377 center in lymph nodes during chronic antigen exposure<sup>64</sup>. Tcy03 (1.37%) specifically  
378 expresses high levels of CD137/4-1BB, which is transiently expressed after TCR-pathway

379 mediated activation<sup>65,66</sup>, and which is used in clinical trials to improve response to TIL therapy  
380 by selecting for 4-1BB expressing cells (NCT02111863). The discriminating feature of Tcy04  
381 (7.00%) is high expression of CD69, without co-expression of inhibitory receptors such as PD-  
382 1 or TIM-3. CD69 is an early T-cell activation marker with transient upregulation after  
383 activation<sup>67</sup>. Recently, it has been shown that tissue resident T-cells can also express this  
384 receptor in the absence of T-cell receptor stimulation<sup>68</sup>. Both Tcy05 (22.63%) and Tcy06  
385 (5.17%) have variable levels of the transcription factor TCF1/TCF7 and the co-stimulatory  
386 molecule CD7, both typically expressed in the 'naïve-like' or 'memory' Tcy subset<sup>69-71</sup>.  
387 Furthermore, Tcy06 shows simultaneous expression of intermediate levels of PD-1, TIM-3 and  
388 CD69. In Tcy07 (6.08%), Tcy08 (6.23%) and Tcy09 (11.99%) increasing levels of expression  
389 of co-inhibitory receptors (PD-1, TIM-3 and VISTA) are observed, suggestive of a more  
390 exhausted/dysfunctional phenotype<sup>69</sup>. Interestingly, the observed proteomic signature of  
391 Tcy06 seems to correspond to an earlier described Tcy population of so-called progenitor  
392 exhausted Tcy at the transcriptomic level, with high expression of TCF7, intermediate levels  
393 of CD69/CXCR5 and TIM-3/PD-1 which are known to be markers of exhaustion correlating  
394 with increasing T-cell dysfunctionality. However, TIM-3/PD-1 are expressed at lower amounts  
395 than in the presumably more dysfunctional subtypes (Tcy07, Tcy08 and Tcy09)<sup>29,30</sup>. Previous  
396 reports suggest that this Tcy subtype also resembles a stem-like population capable of giving  
397 rise to more exhausted progeny as defined by an increasing amount of expression of  
398 exhaustion markers like our Tcy07, 08 and 09 cluster<sup>30,31,36,72</sup>. When looking at the potential  
399 cytotoxicity of these subclusters based on GrB expression, we find only relevant amounts of  
400 expression in Tcy08. This is in line with previous findings which also attribute a higher  
401 proliferative activity to this subtype based on Ki67 expression<sup>72,73</sup>.

402 In addition, using the *in-silico* microdissection and the previously described proteomic  
403 Tcy signatures, we analyzed the possible enrichment of specific subtypes in the different areas  
404 of the tumor. No significant differences could be found for most of the different Tcy, although  
405 an expected trend towards enrichment of exhausted subtypes within the tumor area seemed  
406 to emerge (Fig. 2D). On the contrary, the TCF7 expressing subtypes, i.e., Tcy05 and Tcy06,  
407 were blocked at the TSI and were not detected in the tumor bed, confirming the finding  
408 described in a previous report<sup>31</sup> (Fig. 2D). Finally, comparing RESP vs NRESP, no significant  
409 differences were found in bulk (Suppl. Fig. 6C) and *in-silico* microdissected areas (Suppl. Fig.  
410 6D).

411

#### 412 4. Spatial dynamics of Tcy differentiation

413 In the previous section, only discrete spatial differences could be detected comparing the  
414 enrichment of different Tcy subtypes within the different areas of the tumor. Nonetheless, as  
415 Tcy infiltrate the tumor and are chronically exposed to tumor-specific antigens (tumor-immune  
416 interaction) and to the immune microenvironment (immune-immune interaction), a spatial  
417 differentiation trajectory is expected. We hypothesized that the spatial differences in Tcy  
418 subtype were not completely captured by our previous analysis, largely because of the use of  
419 microdissected areas (TA, TSI and NTA) as opposed to a continuous spatial description from  
420 the non-tumor area towards the tumor area. As such, we further refined the spatial resolution  
421 of our analysis to further explore the tumor-Tcy interaction and Tcy expression profile.

422 First, based on our observation of a trend towards enrichment of the exhausted phenotypes  
423 within the tumor, we evaluated the spatial dynamics of Tcy activation, applying a simplified  
424 model that integrates the simultaneous expression of 4 markers (CD69, OX40, LAG3 and TIM-  
425 3) as previously published<sup>46</sup>. By comparing the average level of activation in the 3 different  
426 microdissected areas, not surprisingly Tcy are significantly more active in the NTA compared

427 to Tcy in the TA (Fig. 2E-F). Furthermore, the same spatial dynamics is observed when  
428 analyzing Tcy activation for each Tcy subtype in the different microdissected areas although  
429 only that of Tcy06 is significant (Fig. 2G).

430 Next, to profile how this level of activation dynamically evolves even in a higher  
431 resolution, the average level of activation of Tcy at specific distances from the tumor edge was  
432 analyzed. This confirmed the largest change in activation status as happening in the TSI at 60  
433 micrometers of the tumor-edge towards the NTA (Fig. 2H). Interestingly, at 180 micrometers  
434 from the tumor-edge towards the NTA the normalized Tcy activation starts decreasing as  
435 indicated by the negative value of the first derivative of the fitted curve (see methods) (Fig.  
436 2H). This suggests that active Tcy accumulate in the vicinity of the tumor edge still within the  
437 NTA. When comparing RESP vs NRESP, the gradient in activation is more pronounced for  
438 RESP patients (Fig. 2I).

439 As we could observe this transition in Tcy activation status, mainly at the TSI, we  
440 expected to see a similar spatial transition in Tcy differentiation. Indeed, when plotting the  
441 probability of each Tcy belonging to any of the proteomic Tcy signatures at different distances  
442 to the tumor edge (see methods), a spatial gradient emerged. It was apparent that Tcy outside  
443 the tumor, far from the edge, are likely to be part of cluster Tcy05. On the contrary, when closer  
444 to the tumor edge, this likelihood decreases, and Tcy are more likely to be part of cluster Tcy06  
445 and Tcy07 (Fig. 3A). Tcy infiltrating the tumor are more likely to be part of Tcy08 and eventually  
446 Tcy09 as they infiltrate deeper in the tumor, very much in line with the results obtained from  
447 our Tcy activation analysis (Fig. 2E-G). This spatial trajectory of Tcy subtype signature from  
448 outside the tumor to inside the tumor (Tcy05 to Tcy09), is also notable by the mean distance  
449 to the tumor edge for each of the Tcy subtypes (Suppl. Fig. 7). This again confirms this non-  
450 random spatial distribution of Tcy. Moreover, when comparing the expression values of  
451 selected markers of activation and exhaustion in Tcy05-09, we observed a gradient in  
452 expression of these markers in these subtypes (Fig. 3B). Based on these results, we  
453 hypothesized these spatial changes in Tcy subcluster signature correlates with a spatial  
454 differentiation trajectory within the tissue and this trajectory in T-cell phenotype and function is  
455 caused by the dynamic process of T-cells infiltrating the tumor from the peritumoral niche. To  
456 further corroborate this spatial behavior, we correlated the spatial distance of Tcy to the tumor  
457 edge with a pseudotime value obtained after cell lineage and pseudotime inference using  
458 Slingshot<sup>52</sup> to a selected number of Tcy subtypes (Fig. 3C-F). Indeed, we could observe a non-  
459 random behavior between the spatial location of Tcy and the pseudotime values, confirming  
460 that Tcy which are deeply infiltrative in the tumor are indeed the more terminally  
461 differentiated/exhausted cells and Tcy outside the tumor are generally more functional/less  
462 exhausted and hence are at the beginning of their differentiation trajectory. In addition, with  
463 this approach, we could further determine the location of the Tcy subset in treatment naïve as  
464 well as anti-PD-1 treated patients<sup>29-31,36</sup>. Our results show a peak in cytotoxicity (as determined  
465 by GrB expression) and proliferation (as determined by Ki67 expression) combined with a  
466 lower TCF7/higher PD-1 expression at the inner border of the TSI compared to the outer rim  
467 of the tumor stroma interface or non-tumoral areas (Fig. 3F).

## 468 469 5. Spatial Tcy macrophage interaction

470 Besides defining the Tcy niche and the Tcy tumor interaction, we were wondering to what  
471 extent an immune-immune interaction (e.g., the interaction between Tcy and other immune  
472 cell types present in the TME) and the composition of the immune cell niche impacts on this  
473 trajectory. Based on our cell composition analysis we found that macrophages are the most  
474 abundant immune cell type in both the TA and the TSI (Fig. 1C).

475 Other groups have shown by using *ex vivo* and/or functional assays that the myeloid  
476 compartment and Tcy closely interact and influence each other in multiple ways, such as,  
477 myeloid cell triggered suppression of Tcy effector function and/or Tcy exhaustion or Tcy-  
478 induced macrophage polarization<sup>74-79</sup>. Nonetheless, *in situ* confirmation of these findings by  
479 spatial analysis is rather limited. We were therefore specifically interested in further  
480 deciphering this Tcy-macrophage interaction.

481

### 482 5.1. Spatial effect of neighboring Tcy on PD-L1 expression in macrophages

483 We first analyzed the correlation between neighboring Tcy and the expression of PD-L1 in  
484 macrophages. PD-L1 expression in macrophages has been described to have predictive value  
485 in patients treated with anti-PD-1 antibodies in melanoma, ovarian cancer, sarcoma and  
486 NSCLC, suggesting that the PD-L1 status of macrophages is important in addition to their mere  
487 presence in the tumor stroma<sup>80-82</sup>. Similar to Tcy activation, we analyzed how the expression  
488 of PD-L1 in both M1-like and M2-like macrophages differs depending on their localization  
489 relative to the tumor. For both types of macrophages, the PD-L1 expression is significantly  
490 lower in the TA when compared to the NTA and the TSI (Fig. 4A). Next, by increasing the  
491 spatial resolution around the tumor edge, we observed a peak in PD-L1 expression close to  
492 the tumor edge outside of the tumor for M1-like and M2-like macrophages (peak at 40  $\mu$ m and  
493 70  $\mu$ m respectively from the tumor edge), with the highest expression observed in M2-like  
494 macrophages (Fig. 4B). Based on the predictive value of PD-L1 expression in macrophages  
495 for checkpoint inhibitors described by others<sup>80-82</sup>, we repeated the analysis only for the anti-  
496 PD-1-treated patients (7 RESP, 8 NRESP). Remarkably, for both types of macrophages, these  
497 differences are only preserved for the subset of RESP patients whereas for the NRESP  
498 patients the differences are not significant (Suppl. Fig. 8). Next, we hypothesized that the  
499 expression of PD-L1 in macrophages is also influenced by the local microenvironment,  
500 specifically by Tcy, for example via interferon-gamma secretion<sup>83,84</sup>. For this analysis, we  
501 calculated the shortest distance to the closest Tcy for all macrophages irrespective of their  
502 location and defined a cut-off value of 100  $\mu$ m to discriminate between macrophages that could  
503 be considered close to at least one Tcy ('Tcy-close') and macrophages that could be  
504 considered far from any Tcy ('Tcy-far'). Comparing PD-L1 expression in these two groups of  
505 macrophages, PD-L1 was found significantly higher in 'Tcy-close' macrophages (Fig. 4D).  
506 Coherently, when analyzing the expression of PD-L1 relative to a gradual increase in distance  
507 to the closest Tcy, we observed a gradual decrease in the level of expression with the distance  
508 away from a Tcy (Fig. 4E). Interestingly, when comparing RESP and NRESP, an inverse  
509 correlation between PD-L1 expression and distance to closest Tcy is only present in the RESP  
510 patients (Fig. 4F).

511 Based on the previous analysis, 2 spatial components influence the expression of PD-  
512 L1 in M1-like and M2-like macrophages: 1) The localization of the macrophage relative to the  
513 tumor, and 2) distance to Tcy, specifically for RESP patients. To evaluate whether both spatial  
514 components have a synergistic effect on PD-L1 expression, we compared the level of PD-L1  
515 in the following 4 groups, both for M1-like and M2-like macrophages: 1) Macrophages close to  
516 the tumor edge and close to Tcy ('Close-Close'; CC), 2) Macrophages close to the tumor edge  
517 but far from Tcy ('Close-Far'; CF), 3) Macrophages far from the tumor edge but close to Tcy  
518 ('Far-Close'; FC), and 4) Macrophages far from the tumor edge and far from Tcy ('Far-Far';  
519 FF). Confirming the previous analysis, both spatial features (distance to tumor edge and  
520 distance to Tcy) were associated with increased expression of PD-L1 (comparing both 'Close-  
521 Far' and 'Far-Close' with 'Far-Far'). As expected, the highest expression is observed in the  
522 'Close-Close' subgroup, suggesting a rather additive effect of both spatial components (Fig.

523 4G). When comparing RESP and NRESP, the significant difference between 'Close-Close'  
524 and 'Far-Far' is only preserved in the RESP patients both in M1-like and M2-like macrophages  
525 (Fig. 4H).

526

## 527 5.2. Spatial effect of neighboring macrophages on Tcy activation

528 Next, we investigated the effect of neighboring macrophages on the activation status of Tcy.  
529 We previously showed a gradual onset of exhaustion as Tcy infiltrate the tumor (Fig. 2E).  
530 Similar to the influence of neighboring Tcy on the expression of PD-L1 in macrophages, we  
531 explored how this spatial behavior of Tcy activation is affected by the presence of  
532 macrophages close to Tcy. To start, using the shortest distance to the closest macrophage,  
533 we separated Tcy into 'M1 close'/'M2 close' Tcy and 'M1 far'/'M2 far' Tcy using 30  $\mu$ m as  
534 threshold to define 'close' vs 'far' (Fig. 5A). We found that Tcy close to M1-like macrophages  
535 are significantly more exhausted than Tcy that are far away from M1-like macrophages, which  
536 was not significant for M2-like macrophages (Fig. 5C). When comparing RESP with NRESP,  
537 remarkable differences emerge. Whereas Tcy close to M1-like macrophages are significantly  
538 more exhausted compared to Tcy far from M1-like macrophages in the RESP patients, no  
539 significant difference in level of activation of Tcy in relation to macrophages is observed in the  
540 NRESP patients (Fig. 5B and 5D).

541 Finally, we combined both spatial features (location of Tcy relative to the tumor-edge  
542 and distance to closest M1/M2-like macrophage) comparing the level of Tcy activation in the  
543 following 4 groups: 1) Tcy close to the tumor edge and close to macrophage ('Close-Close'),  
544 2) Tcy close to the tumor edge but far from macrophage ('Close-Far'), 3) Tcy far from the tumor  
545 edge but close to macrophage ('Far-Close') and 4) Tcy far from the tumor edge and far from  
546 macrophage ('Far-Far'). Both for M1- and M2-like macrophages, the 2 spatial features work  
547 synergistically in exhausting Tcy with the highest exhaustion present in Tcy close to the tumor  
548 edge and close to macrophages (Fig. 5E). Similarly, when comparing the level of exhaustion  
549 in these 4 different spatial groups of Tcy within RESP and NRESP, the significant difference  
550 is only preserved in the RESP for M1-like macrophages, showing again the highest exhaustion  
551 in 'Close-Close' Tcy (Fig. 5F).

552

## 553 6. Spatial biomarkers predicting response to anti-PD-1 therapy

554 The ultimate goal of multiplex immunohistochemistry is to serve as a predictive tool for patients  
555 undergoing immune checkpoint inhibitor therapy. We therefore explored to which extent  
556 spatially extracted features can be used to predict response to anti-PD-1 treatment.  
557 On one hand, we observed significant spatial differences in the expression of PD-L1 in  
558 macrophages between RESP and NRESP (Fig. 4). On the other hand, the predictive value of  
559 bulk PD-L1 expression in melanoma has not yet been shown to have predictive ability in  
560 serving as a clinical biomarker<sup>85</sup>. This is in contrast to other immune checkpoint inhibitor  
561 sensitive diseases where the "bulky analysis" of PD-L1 is used as a stratifying factor for anti-  
562 PD-1 therapy<sup>80-82</sup>. We were therefore wondering whether adding spatial information would  
563 further improve the predictive value of PD-L1 expression. First, considering the average PD-  
564 L1 expression in the entire sample ("Bulk analysis") carries, as expected, a rather low  
565 predictive value (AUC = 0.73, Fig. 6A top). When comparing the PD-L1 expression in M1-like  
566 and M2-like macrophages between RESP and NRESP ("Single-cell, non-spatial"), we  
567 observed an increase in AUC only for the expression in M1-like macrophages (AUC = 0.75,  
568 Fig. 6A center). By adding spatial information and focusing on the expression of PD-L1  
569 exclusively in macrophages that are close to the tumor edge and close to Tcy, we observed a

570 further increase in the predictive value in M1-like macrophages reaching an AUC of 0.93 (Fig.  
571 6A bottom).

572         The same improvement in the predictive value of Tcy activation could be obtained by  
573 adding spatial information. Considering the differences in spatial dynamics in Tcy activation  
574 between RESP and NRESP (Fig. 2I), and by comparing the difference in Tcy activation  
575 between TA and NTA, it was apparent that RESP patients were poorly separated from NRESP  
576 patients (AUC 0.7, Fig. 6B). However, when considering only those Tcy that are close to M1-  
577 like macrophages and comparing the level of Tcy activation, the predictive value increased,  
578 reaching an AUC of 0.86 (Fig. 6C).

579 **Discussion**

580 The race to identify biomarkers to predict a response to checkpoint inhibition therapy in  
581 patients with malignant melanoma has produced a plethora of potential candidates over the  
582 past few years<sup>86</sup>. Nevertheless, for melanoma, none of these therapies has been implemented  
583 in clinical practice as they have not elicited sufficient predictive power thus far. In contrast to  
584 targeted therapy, where the presence of a single driver mutation poses a simple and effective  
585 marker for selecting patients most likely to respond to the corresponding therapy, in  
586 immunotherapy treated patients' responses are vastly more complex. Obviously, the immune  
587 microenvironment poses a multicellular system which amongst others is constituted of multiple  
588 types of inflammatory cells, each of them present in many different functional states and  
589 locations. It has become obvious that to adequately interrogate the tumor immune ecosystem,  
590 the use of single cell technologies that include as many parameters as possible is required.  
591 Importantly these technologies should also enable to capture the spatial distribution of the  
592 different cell types and shed light on their spatial relationships. In this study, we have employed  
593 multiplexed immunohistochemistry to create a detailed immune landscape of untreated  
594 metastatic melanoma, with a focus on the role of Tcy and their spatial interactions with other  
595 components of the tumor microenvironment.

596 Previous reports based on low-plex immunohistochemistry have found preliminary  
597 evidence that the location, and not just the composition of the inflammatory cells is associated  
598 with functional differences that are fundamental for an anti-tumoral immune response<sup>87-92</sup>. With  
599 our high-plex spatial technique, we were able to precisely localize each inflammatory cell in  
600 the tissue. This allowed us to study the evolution of some specific functional states in relation  
601 to the spatial distribution of these cells. In particular, we identified Tcy subtypes based on a  
602 marker profile described in previous literature<sup>29</sup> and identified their location in the tissue. The  
603 approach we used could be applied on much larger numbers of cells compared to other single  
604 cell techniques e.g., scRNA-seq. Moreover, by applying novel spatial analysis tools in  
605 combination with our previously described Tcy activation score<sup>46</sup>, we visualized an increase of  
606 Tcy exhaustion along a gradient that ran perpendicular from outside the tumor, across the TSI  
607 towards the inside of the tumor.

608 In addition, by studying cell-cell interactions using neighborhood analyses, we have  
609 demonstrated that PD-L1 expression is a discriminator for response in our melanoma cohort  
610 when analyzed in the spatial context. Our findings suggest that, at least in melanoma, PD-L1  
611 expression should not be analyzed on bulk level but using technologies with much higher  
612 resolution. Specifically, when integrating spatial information and cell-cell interaction between  
613 Tcy and macrophages, the technique we employed allowed us to further decipher differences  
614 between RESP and NRESP. It is known that PD-L1 expression in macrophages is induced by  
615 an interferon-gamma rich environment secreted by lymphocytes<sup>83,84</sup>, and that PD-L1  
616 expression by macrophages is typically present at the TSI<sup>93</sup>. Our data demonstrates that in  
617 RESP patients specifically, PD-L1 expression levels are very high in M1-like and M2-like  
618 macrophages at the TSI followed by a rapid decrease in expression inside the TA. When  
619 investigating the level of Tcy activation, the opposite trend is evident. The closer Tcy are  
620 located to M1-like and M2-like macrophages at the TSI, the larger the decrease in activation  
621 markers, hereby suggesting that in RESP patients, PD-L1 expression and Tcy activation follow  
622 a more orderly spatial regulation while in NRESP patients these are more chaotic.

623 In summary our data show the feasibility of high-dimensional mIHC as a valuable  
624 technique in the armamentarium of single cell analysis in the quest for biomarkers associated  
625 with response to anti-PD-1 therapy in melanoma. We demonstrate that marker expression on  
626 cellular components of the tumor microenvironment is a very dynamic process, and that spatial

627 information is crucial in identifying relevant cell-cell interactions and dynamics of marker  
628 expression. Given the complexity of the mechanisms of an immune response we believe that  
629 integrating multiple techniques will be necessary to gain a deeper understanding of what  
630 makes immunotherapy successful.

631 **References**

- 632 1. Robert, C. *et al.* Ipilimumab plus Dacarbazine for Previously Untreated Metastatic  
633 Melanoma. *N. Engl. J. Med.* **364**, (2011).
- 634 2. Robert, C. *et al.* Pembrolizumab versus Ipilimumab in Advanced Melanoma. *N. Engl. J.*  
635 *Med.* **372**, (2015).
- 636 3. Robert, C. *et al.* Nivolumab in Previously Untreated Melanoma without BRAF Mutation  
637 . *N. Engl. J. Med.* **372**, (2015).
- 638 4. Larkin, J. *et al.* Combined Nivolumab and Ipilimumab or Monotherapy in Untreated  
639 Melanoma. *N. Engl. J. Med.* **373**, (2015).
- 640 5. Lu, M. *et al.* A genomic signature for accurate classification and prediction of clinical  
641 outcomes in cancer patients treated with immune checkpoint blockade immunotherapy.  
642 *Sci. Rep.* **10**, (2020).
- 643 6. Snyder, A. & al., *et.* Genetic basis for clinical response to CTLA-4 blockade in  
644 melanoma. *N. Engl. J. Med.* **371**, 2189–2199 (2014).
- 645 7. Rizvi, N. A. Cancer immunology. Mutational landscape determines sensitivity to PD-1  
646 blockade in non-small cell lung cancer. *Science (80-. )*. **348**, 124–128 (2015).
- 647 8. Johnson, D. B. *et al.* Melanoma-specific MHC-II expression represents a tumour-  
648 autonomous phenotype and predicts response to anti-PD-1/PD-L1 therapy. *Nat.*  
649 *Commun.* **7**, (2016).
- 650 9. Gao, J. *et al.* Loss of IFN- $\gamma$  Pathway Genes in Tumor Cells as a Mechanism of  
651 Resistance to Anti-CTLA-4 Therapy. *Cell* **167**, (2016).
- 652 10. Hargadon, K. M., Györffy, B. & McGee, T. J. Genomic and transcriptional changes in  
653 IFN $\gamma$  pathway genes are putative biomarkers of response to ipilimumab immunotherapy  
654 in melanoma patients. *Expert Rev. Clin. Immunol.* **16**, (2020).
- 655 11. Weiss, S. A. *et al.* Impact of aging on host immune response and survival in melanoma:  
656 An analysis of 3 patient cohorts. *J. Transl. Med.* **14**, (2016).
- 657 12. Horn, S. *et al.* Tumor CDKN2A-associated JAK2 loss and susceptibility to  
658 immunotherapy resistance. *J. Natl. Cancer Inst.* **110**, (2018).
- 659 13. Zaretsky, J. M. *et al.* Mutations Associated with Acquired Resistance to PD-1 Blockade  
660 in Melanoma. *N. Engl. J. Med.* **375**, (2016).
- 661 14. Sade-Feldman, M. *et al.* Resistance to checkpoint blockade therapy through inactivation  
662 of antigen presentation. *Nat. Commun.* **8**, (2017).
- 663 15. Tumei, P. C. *et al.* PD-1 blockade induces responses by inhibiting adaptive immune  
664 resistance. *Nature* **515**, (2014).
- 665 16. Chen, P. L. *et al.* Analysis of immune signatures in longitudinal tumor samples yields  
666 insight into biomarkers of response and mechanisms of resistance to immune  
667 checkpoint blockade. *Cancer Discov.* **6**, (2016).
- 668 17. Griss, J. *et al.* B cells sustain inflammation and predict response to immune checkpoint  
669 blockade in human melanoma. *Nat. Commun.* **10**, (2019).
- 670 18. Cabrita, R. *et al.* Tertiary lymphoid structures improve immunotherapy and survival in  
671 melanoma. *Nature* **577**, (2020).
- 672 19. Helmink, B. A. *et al.* B cells and tertiary lymphoid structures promote immunotherapy  
673 response. *Nature* **577**, (2020).
- 674 20. Auslander, N. *et al.* Robust prediction of response to immune checkpoint blockade  
675 therapy in metastatic melanoma. *Nat. Med.* **24**, (2018).
- 676 21. Hugo, W. *et al.* Genomic and Transcriptomic Features of Response to Anti-PD-1  
677 Therapy in Metastatic Melanoma. (2016). doi:10.1016/j.cell.2016.02.065
- 678 22. Ayers, M. *et al.* IFN- $\gamma$ -related mRNA profile predicts clinical response to PD-1 blockade.

- 679 *J. Clin. Invest.* **127**, (2017).
- 680 23. Prat, A. *et al.* Immune-related gene expression profiling after PD-1 blockade in non-  
681 small cell lung carcinoma, head and neck squamous cell carcinoma, and melanoma.  
682 *Cancer Res.* **77**, (2017).
- 683 24. Riaz, N. *et al.* Tumor and Microenvironment Evolution during Immunotherapy with  
684 Nivolumab. (2017). doi:10.1016/j.cell.2017.09.028
- 685 25. Long, G. V. *et al.* Combined BRAF and MEK Inhibition versus BRAF Inhibition Alone in  
686 Melanoma. *N. Engl. J. Med.* **371**, (2014).
- 687 26. Grob, J. J. *et al.* Comparison of dabrafenib and trametinib combination therapy with  
688 vemurafenib monotherapy on health-related quality of life in patients with unresectable  
689 or metastatic cutaneous BRAF Val600-mutation-positive melanoma (COMBI-v): Results  
690 of a phase 3, open-label, randomised trial. *Lancet Oncol.* **16**, (2015).
- 691 27. Ascierto, P. A. *et al.* Cobimetinib combined with vemurafenib in advanced BRAFV600-  
692 mutant melanoma (coBRIM): updated efficacy results from a randomised, double-blind,  
693 phase 3 trial. *Lancet Oncol.* **17**, (2016).
- 694 28. Dummer, R. *et al.* Encorafenib plus binimetinib versus vemurafenib or encorafenib in  
695 patients with BRAF-mutant melanoma (COLUMBUS): a multicentre, open-label,  
696 randomised phase 3 trial. *Lancet Oncol.* **19**, (2018).
- 697 29. Sade-Feldman, M. *et al.* Defining T Cell States Associated with Response to Checkpoint  
698 Immunotherapy in Melanoma. *Cell* **175**, 998–1013 (2018).
- 699 30. Kallies, A., Zehn, D. & Utzschneider, D. T. Precursor exhausted T cells: key to  
700 successful immunotherapy? *Nature Reviews Immunology* **20**, (2020).
- 701 31. Siddiqui, I. *et al.* Intratumoral Tcf1 + PD-1 + CD8 + T Cells with Stem-like Properties  
702 Promote Tumor Control in Response to Vaccination and Checkpoint Blockade  
703 Immunotherapy. *Immunity* **50**, (2019).
- 704 32. Simon, S. *et al.* PD-1 and TIGIT coexpression identifies a circulating CD8 T cell subset  
705 predictive of response to anti-PD-1 therapy. *J. Immunother. Cancer* **8**, (2020).
- 706 33. Spencer Wei. Distinct Cellular Mechanisms Underlie Anti-CTLA-4 and Anti-PD-1  
707 Checkpoint Blockade. *Cell* **170**, 1120-1125.e17 (2017).
- 708 34. Kurtulus, S., Madi, A., Kuchroo, V. K., Regev, A. & Correspondence, A. C. A. Checkpoint  
709 Blockade Immunotherapy Induces Dynamic Changes in PD-1-CD8 + Tumor-Infiltrating  
710 T Cells. *Immunity* **50**, 181-194.e6 (2019).
- 711 35. Wu, T. D. *et al.* Peripheral T cell expansion predicts tumour infiltration and clinical  
712 response. *Nature* **579**, (2020).
- 713 36. Miller, B. C. *et al.* Subsets of exhausted CD8+ T cells differentially mediate tumor control  
714 and respond to checkpoint blockade. *Nat. Immunol.* **20**, (2019).
- 715 37. Efremova, M., Vento-Tormo, M., Teichmann, S. A. & Vento-Tormo, R. CellPhoneDB:  
716 inferring cell–cell communication from combined expression of multi-subunit ligand–  
717 receptor complexes. *Nat. Protoc.* **15**, (2020).
- 718 38. Browaeys, R., Saelens, W. & Saeys, Y. NicheNet: modeling intercellular communication  
719 by linking ligands to target genes. *Nat. Methods* **17**, (2020).
- 720 39. Bolognesi, M. M. *et al.* Multiplex Staining by Sequential Immunostaining and Antibody  
721 Removal on Routine Tissue Sections. *J. Histochem. Cytochem.* **65**, (2017).
- 722 40. Eisenhauer, E. A. *et al.* New response evaluation criteria in solid tumours: Revised  
723 RECIST guideline (version 1.1). *Eur. J. Cancer* **45**, (2009).
- 724 41. Smyth, G. K. limma: Linear Models for Microarray Data. in *Bioinformatics and*  
725 *Computational Biology Solutions Using R and Bioconductor* (2005). doi:10.1007/0-387-  
726 29362-0\_23

- 727 42. Våremo, L., Nielsen, J. & Nookaew, I. Enriching the gene set analysis of genome-wide  
728 data by incorporating directionality of gene expression and combining statistical  
729 hypotheses and methods. *Nucleic Acids Res.* **41**, (2013).
- 730 43. Liberzon, A. *et al.* The Molecular Signatures Database Hallmark Gene Set Collection.  
731 *Cell Syst.* **1**, (2015).
- 732 44. Newman, A. M. *et al.* Determining cell type abundance and expression from bulk tissues  
733 with digital cytometry. *Nat. Biotechnol.* **37**, (2019).
- 734 45. Tirosh, I. *et al.* Dissecting the multicellular ecosystem of metastatic melanoma by single-  
735 cell RNA-seq. *Science (80-. )*. **352**, (2016).
- 736 46. Bosisio, F. M. *et al.* Functional heterogeneity of lymphocytic patterns in primary  
737 melanoma dissected through single-cell multiplexing. *Elife* **9**, (2020).
- 738 47. Pau, G., Fuchs, F., Sklyar, O., Boutros, M. & Huber, W. EBImage-an R package for  
739 image processing with applications to cellular phenotypes. *Bioinformatics* **26**, (2010).
- 740 48. Caicedo, J. C. *et al.* Data-analysis strategies for image-based cell profiling. *Nat.*  
741 *Methods* **14**, (2017).
- 742 49. Levine, J. H. *et al.* Data-Driven Phenotypic Dissection of AML Reveals Progenitor-like  
743 Cells that Correlate with Prognosis. *Cell* **162**, (2015).
- 744 50. Van Gassen, S. *et al.* FlowSOM: Using self-organizing maps for visualization and  
745 interpretation of cytometry data. *Cytom. Part A* **87**, (2015).
- 746 51. Parra, E. R. Methods to Determine and Analyze the Cellular Spatial Distribution  
747 Extracted From Multiplex Immunofluorescence Data to Understand the Tumor  
748 Microenvironment. *Front. Mol. Biosci.* **8**, (2021).
- 749 52. Street, K. *et al.* Slingshot: Cell lineage and pseudotime inference for single-cell  
750 transcriptomics. *BMC Genomics* **19**, (2018).
- 751 53. Haghverdi, L., Buettner, F. & Theis, F. J. Diffusion maps for high-dimensional single-cell  
752 analysis of differentiation data. *Bioinformatics* **31**, (2015).
- 753 54. Heidegger, S. *et al.* Role of melanoma cell-intrinsic RIG-I and STING signaling for  
754 checkpoint inhibitor-mediated anticancer immunity. *J. Clin. Oncol.* **36**, (2018).
- 755 55. Such, L. *et al.* Targeting the innate immunoreceptor RIG-I overcomes melanoma-  
756 intrinsic resistance to T cell immunotherapy. *J. Clin. Invest.* **140**, (2020).
- 757 56. Xue, Z. *et al.* MAP3K1 and MAP2K4 mutations are associated with sensitivity to MEK  
758 inhibitors in multiple cancer models. *Cell Res.* **28**, (2018).
- 759 57. Truong, K. L. *et al.* Killer-like receptors and GPR56 progressive expression defines  
760 cytokine production of human CD4+ memory T cells. *Nat. Commun.* **10**, (2019).
- 761 58. Oliver, J. L., Alexander, M. P., Norrod, A. G., Mullins, I. M. & Mullins, D. W. Differential  
762 expression and tumor necrosis factor-mediated regulation of  
763 TNFRSF11b/osteoprotegerin production by human melanomas. *Pigment Cell*  
764 *Melanoma Res.* **26**, (2013).
- 765 59. Matoska, J., Wahlstrom, T., Vaheri, A., Bizik, J. & Grofova, M. Tumor-associated alpha-  
766 2-macroglobulin in human melanomas. *Int. J. Cancer* **41**, (1988).
- 767 60. Burgess, E. F. *et al.* Prostate cancer serum biomarker discovery through proteomic  
768 analysis of alpha-2 macroglobulin protein complexes. *Proteomics - Clin. Appl.* **2**, (2008).
- 769 61. Simpson, A., Petnga, W., Macaulay, V. M., Weyer-Czernilofsky, U. & Bogenrieder, T.  
770 Insulin-Like Growth Factor (IGF) Pathway Targeting in Cancer: Role of the IGF Axis and  
771 Opportunities for Future Combination Studies. *Target. Oncol.* **12**, (2017).
- 772 62. Yamada, K. *et al.* MFG-E8 drives melanoma growth by stimulating mesenchymal  
773 stromal cell-induced angiogenesis and M2 polarization of tumor-associated  
774 macrophages. *Cancer Res.* **76**, (2016).

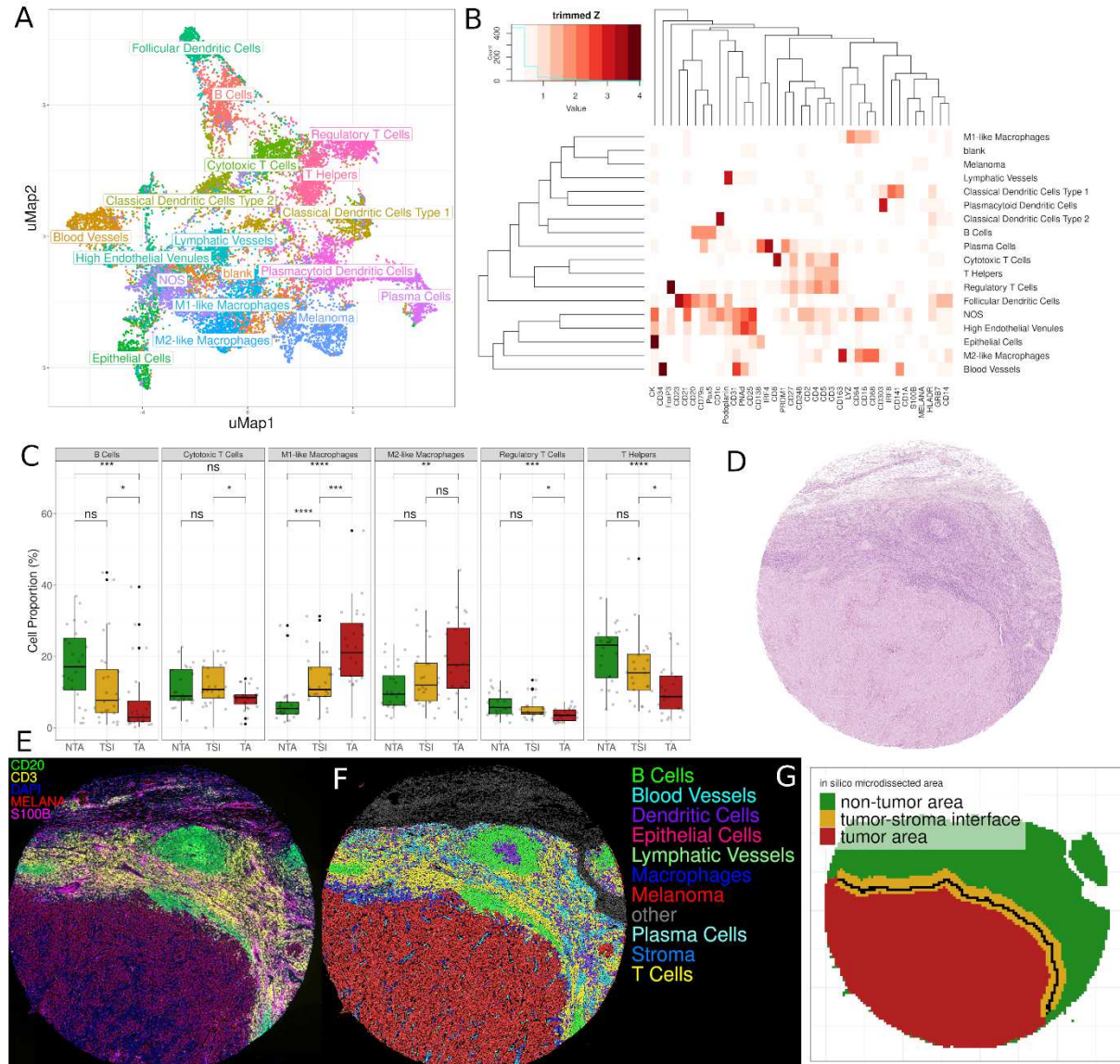
- 775 63. Cirillo, N. *et al.* Characterisation of the cancer-associated glucocorticoid system: Key  
776 role of 11 $\beta$ -hydroxysteroid dehydrogenase type 2. *Br. J. Cancer* **117**, (2017).
- 777 64. Valentine, K. M. & Hoyer, K. K. CXCR5+ CD8 T cells: Protective or pathogenic?  
778 *Frontiers in Immunology* **10**, (2019).
- 779 65. Reithofer, M. *et al.* 4-1BB costimulation promotes bystander activation of human CD8  
780 T cells. *Eur. J. Immunol.* **51**, (2021).
- 781 66. Watts, T. H. TNF/TNFR family members in costimulation of T cell responses. *Annual*  
782 *Review of Immunology* **23**, (2005).
- 783 67. Cibrián, D. & Sánchez-Madrid, F. CD69: from activation marker to metabolic  
784 gatekeeper. *European Journal of Immunology* **47**, (2017).
- 785 68. Edwards, J. *et al.* CD103+ tumor-resident CD8+ T cells are associated with improved  
786 survival in immunotherapy-naïve melanoma patients and expand significantly during  
787 anti-PD-1 treatment. *Clin. Cancer Res.* **24**, (2018).
- 788 69. van der Leun, A. M., Thommen, D. S. & Schumacher, T. N. CD8+ T cell states in human  
789 cancer: insights from single-cell analysis. *Nature Reviews Cancer* **20**, (2020).
- 790 70. Qian, J. *et al.* A pan-cancer blueprint of the heterogeneous tumor microenvironment  
791 revealed by single-cell profiling. *Cell Res.* **30**, (2020).
- 792 71. Aandahl, E. M. *et al.* CD7 Is a Differentiation Marker That Identifies Multiple CD8 T Cell  
793 Effector Subsets. *J. Immunol.* **170**, (2003).
- 794 72. Beltra, J. C. *et al.* Developmental Relationships of Four Exhausted CD8+ T Cell Subsets  
795 Reveals Underlying Transcriptional and Epigenetic Landscape Control Mechanisms.  
796 *Immunity* **52**, (2020).
- 797 73. Chu, T. & Zehn, D. Charting the Roadmap of T Cell Exhaustion. *Immunity* **52**, (2020).
- 798 74. Awad, R. M., De Vlaeminck, Y., Maebe, J., Goyvaerts, C. & Breckpot, K. Turn Back the  
799 TIME: Targeting Tumor Infiltrating Myeloid Cells to Revert Cancer Progression.  
800 *Frontiers in immunology* **9**, (2018).
- 801 75. De Vlaeminck, Y., González-Rascón, A., Goyvaerts, C. & Breckpot, K. Cancer-  
802 associated myeloid regulatory cells. *Front. Immunol.* **7**, (2016).
- 803 76. Zhang, W. *et al.* CD8+ T-cell immunosurveillance constrains lymphoid premetastatic  
804 myeloid cell accumulation. *Eur. J. Immunol.* **45**, (2015).
- 805 77. Braun, D. A. *et al.* Progressive immune dysfunction with advancing disease stage in  
806 renal cell carcinoma. *Cancer Cell* **39**, (2021).
- 807 78. Peranzoni, E. *et al.* Macrophages impede CD8 T cells from reaching tumor cells and  
808 limit the efficacy of anti-PD-1 treatment. *Proc. Natl. Acad. Sci. U. S. A.* **115**, (2018).
- 809 79. Suarez, G. V. *et al.* PD-1/PD-L1 Pathway Modulates Macrophage Susceptibility to  
810 Mycobacterium tuberculosis Specific CD8+ T cell Induced Death. *Sci. Rep.* **9**, (2019).
- 811 80. Lin, H. *et al.* Host expression of PD-L1 determines efficacy of PD-L1 pathway blockade-  
812 mediated tumor regression. *J. Clin. Invest.* **128**, (2018).
- 813 81. Keung, E. Z. *et al.* Correlative analyses of the SARC028 trial reveal an association  
814 between sarcoma-associated immune infiltrate and response to pembrolizumab. *Clin.*  
815 *Cancer Res.* **26**, (2020).
- 816 82. Liu, Y. *et al.* Immune cell PD-L1 colocalizes with macrophages and is associated with  
817 outcome in PD-1 pathway blockade therapy. *Clin. Cancer Res.* **26**, (2020).
- 818 83. Abiko, K. *et al.* IFN- $\gamma$  from lymphocytes induces PD-L1 expression and promotes  
819 progression of ovarian cancer. *Br. J. Cancer* **112**, (2015).
- 820 84. Qian, J. *et al.* The IFN- $\gamma$ /PD-L1 axis between T cells and tumor microenvironment: Hints  
821 for glioma anti-PD-1/PD-L1 therapy. *J. Neuroinflammation* **15**, (2018).
- 822 85. Wolchok, J. D. *et al.* Overall Survival with Combined Nivolumab and Ipilimumab in

- 823 Advanced Melanoma. *N. Engl. J. Med.* **377**, (2017).
- 824 86. Garutti, M. *et al.* Find the flame: Predictive biomarkers for immunotherapy in melanoma.  
825 *Cancers* **13**, (2021).
- 826 87. Ménétrier-Caux, C., Gobert, M. & Caux, C. Differences in tumor regulatory T-cell  
827 localization and activation status impact patient outcome. *Cancer Research* **69**, (2009).
- 828 88. Penter, L. *et al.* Localization-associated immune phenotypes of clonally expanded  
829 tumor-infiltrating T cells and distribution of their target antigens in rectal cancer.  
830 *Oncoimmunology* **8**, (2019).
- 831 89. Egelston, C. A. *et al.* Resident memory CD8+ T cells within cancer islands mediate  
832 survival in breast cancer patients. *JCI Insight* **4**, (2019).
- 833 90. Li, X. *et al.* Infiltration of CD8 + T cells into tumor cell clusters in triple-negative breast  
834 cancer. *Proc. Natl. Acad. Sci. U. S. A.* **116**, (2019).
- 835 91. Stromnes, I. M., Hulbert, A., Pierce, R. H., Greenberg, P. D. & Hingorani, S. R. T-cell  
836 localization, activation, and clonal expansion in human pancreatic ductal  
837 adenocarcinoma. *Cancer Immunol. Res.* **5**, (2017).
- 838 92. Rasmusson, A. *et al.* Immunogradient Indicators for Antitumor Response Assessment  
839 by Automated Tumor-Stroma Interface Zone Detection. *Am. J. Pathol.* **190**, (2020).
- 840 93. Bindea, G. *et al.* Spatiotemporal dynamics of intratumoral immune cells reveal the  
841 immune landscape in human cancer. *Immunity* **39**, (2013).

842 **Competing interests**

843 The authors declare no competing interests.

## Figures and legends



845

846

847

848

849

850

851

852

853

854

855

856

857

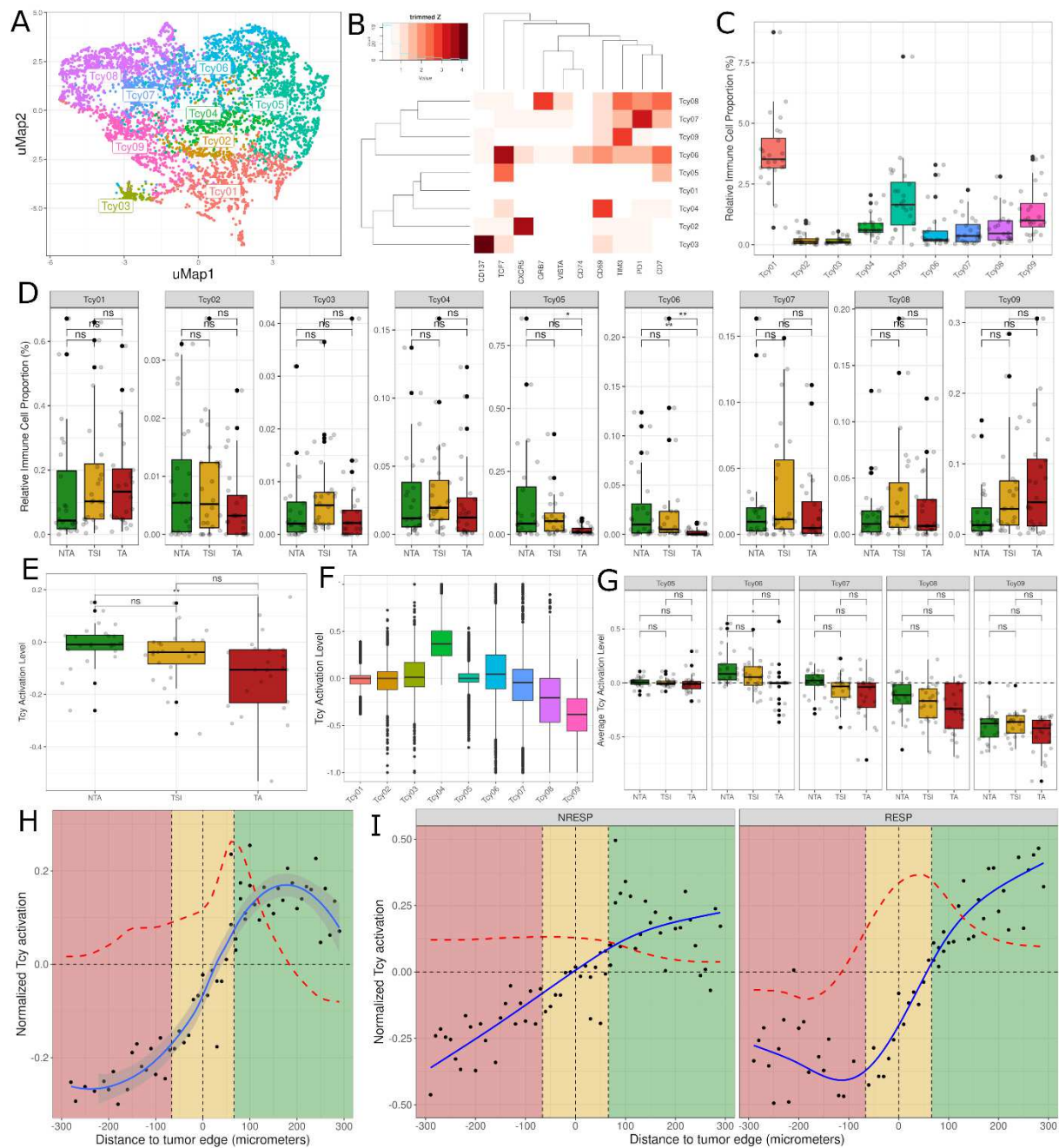
858

859

860

861

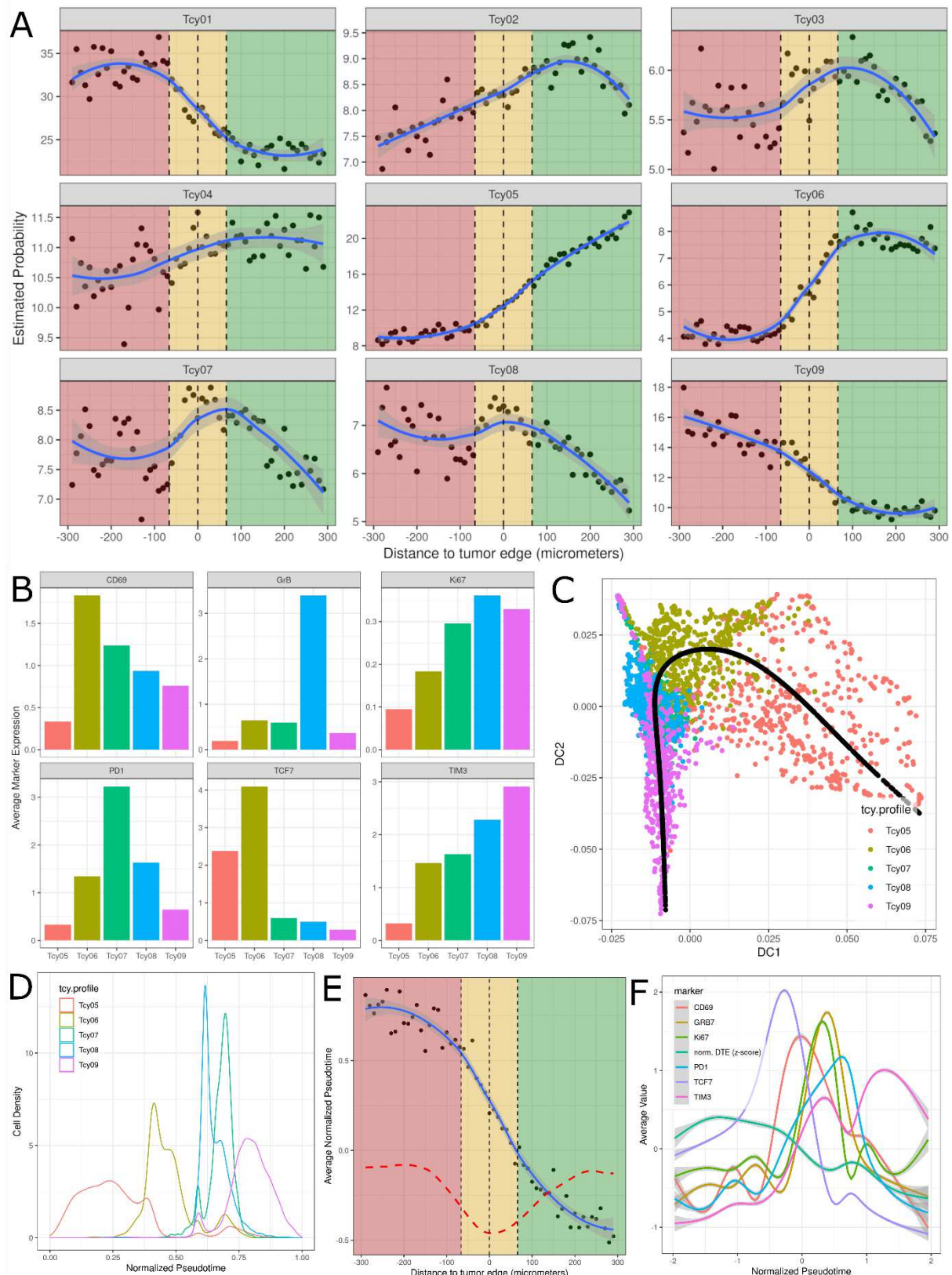
**Figure 1 - Phenotypic identification and in-silico microdissection.** **A)** uMAP showing the 18 different cell phenotypes identified during phenotypic clustering. The colors in the uMAP represent the populations after manual annotation of the 67 clusters obtained with the preselected 37 protein markers. **B)** Heatmap showing the protein signatures of the different cell phenotypes: rows represent identified cell types, columns represent protein markers. The score inside each cell of the matrix indicates the average expression of the marker in the identified population. **C)** Cell composition analysis of selected cell phenotypes comparing the relative proportion of immune cells in the different *in-silico* microdissected areas (NTA: Non-tumor area, TSI: Tumor-stroma interface, TA: Tumor area), using pairwise Wilcoxon test. Representative core from sample MEL9 from patient PT7 with hematoxylin and eosin (H&E) **(D)**, composite fluorescent image of 4 markers (+DAPI) after image processing **(E)**, digital reconstruction of the core highlighting the phenotypic identify of each individual cell **(F)**, and *in-silico* microdissection into 3 areas and the tumor edge (solid black line) within the TSI **(G)**. ns: Not Significant, \* p value < 0.05, \*\* p value < 0.01, \*\*\* p value < 0.001, \*\*\*\* p value < 0.0001.



862  
863  
864  
865  
866  
867  
868  
869  
870  
871  
872  
873  
874  
875  
876

**Figure 2 - Profiling of cytotoxic T-cells: cytometry and activation.** **A)** uMAP showing the 9 different Tcy subtypes identified during Tcy clustering. The colors represent the populations after manual annotation of the 34 clusters identified by KMeans with the selected 10 markers. **B)** Heatmap showing the protein signatures of the different Tcy subtypes: rows represent identified Tcy subtypes, columns represent protein markers. The score inside each cell of the matrix represents the average expression of the marker in the subtype. **C)** Relative immune cell proportion of different Tcy subtypes. **D)** Cell composition analysis of Tcy subtypes comparing the relative proportion within Tcy in the different *in-silico* microdissected areas (NTA: Non-tumor area, TSI: Tumor-stroma interface, TA: Tumor area), using pairwise Wilcoxon test. **E)** Average activation of Tcy in the different *in-silico* microdissected areas (NTA: Non-tumor area, TSI: Tumor-stroma interface, TA: Tumor area), using pairwise t-test. **F)** Boxplots representing the activation of different selected Tcy subtypes. **G)** Boxplots representing the activation of the different subtypes within the different *in-silico* microdissected areas using pairwise t-test. **H)** Activation gradients around the tumor-edge (all patients). **I)** Activation gradient plots for NRESP and RESP patients.

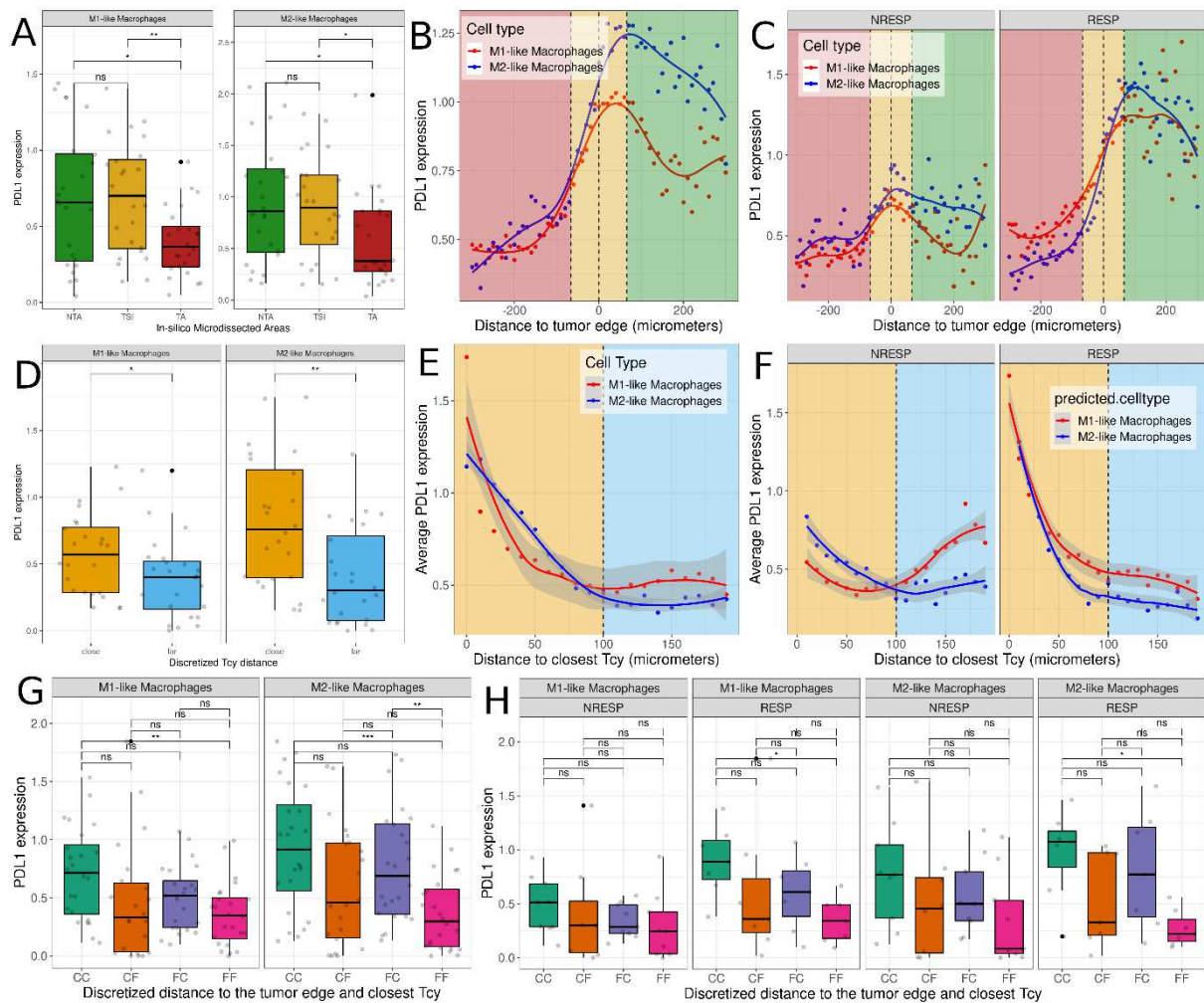
877 Green-shaded area represents the non-tumor area, gold-shaded area represents the tumor-  
878 stroma-interface, red-shaded area represents the tumor-area. Each black dot represents the  
879 average activation level of the Tcy at a given discretized distance from the tumor edge. The  
880 blue line represents the curve fitting for the population of black dots. The red dashed line  
881 represents the first order derivative of the blue line. I) Activation gradients around the tumor-  
882 edge (RESP: responders vs NRESP: non-responders). ns: Not Significant, \*\* p value < 0.01.  
883



884  
 885  
 886  
 887  
 888  
 889

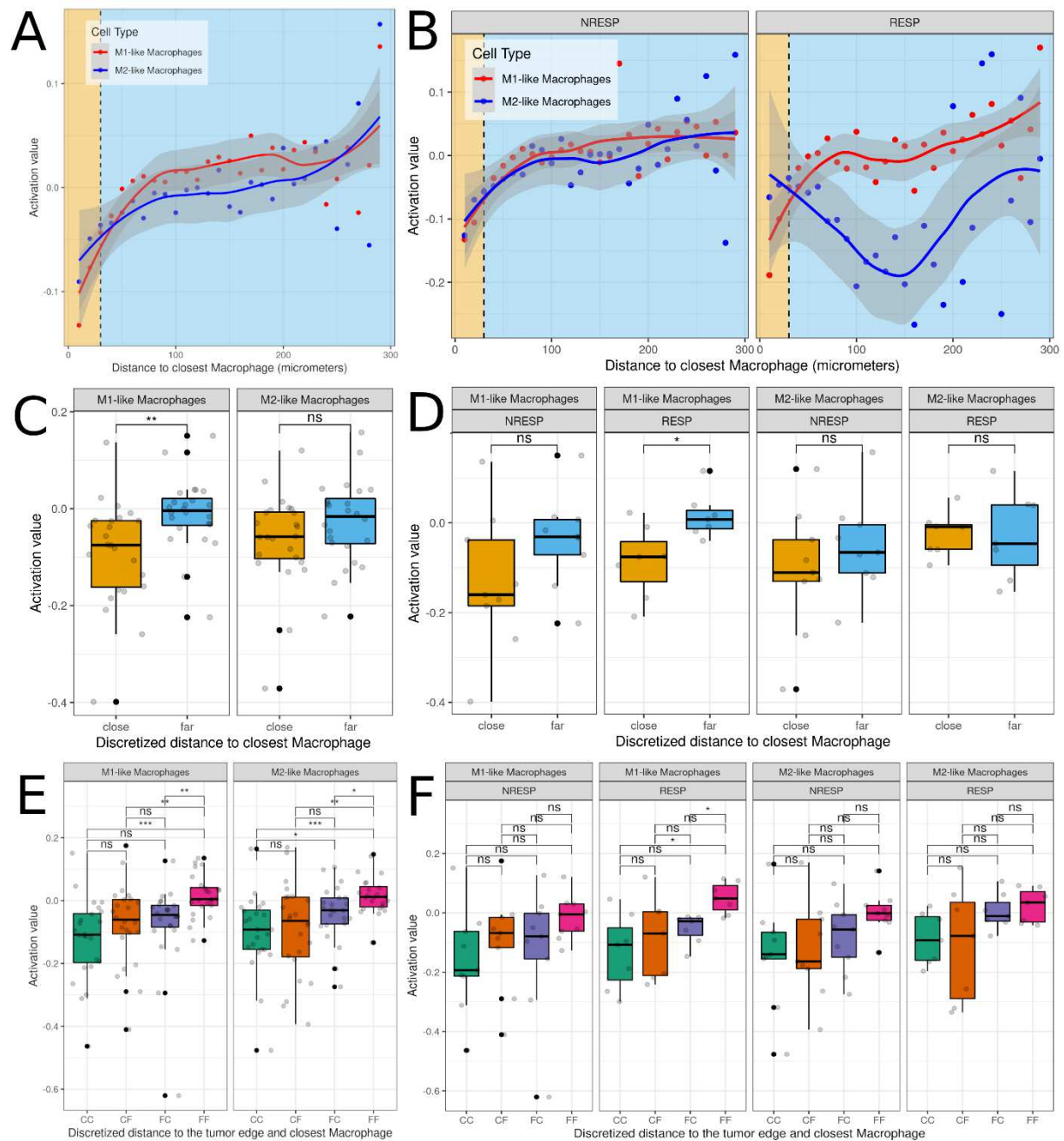
**Figure 3 - Profiling of cytotoxic T-cells: Lineage.** **A)** Probability gradients around the tumor-stroma interface (TSI). Green-shaded area represents the non-tumor area, gold-shaded area represents the TSI, red-shaded area represents the tumor-area. Black dots represent the estimated probability of a Tcy in that region to belong to any of the subtypes. The blue curve represents the curve fitting for that cloud of dots. **B)** Barplots showing the average expression

890 of 6 pre-selected markers (CD69, GrB, Ki67, PD-1, TCF7, and TIM3) for a subset of the  
891 identified Tcy subtypes (Tcy05:Tcy09). **C)** Diffusion map representing the projection of the  
892 trajectory described by the pseudotime analysis (black line). The scatter plot is colored by the  
893 different pre-selected Tcy subtypes (Tcy05:Tcy09). **D)** Density plot of the Tcy subtypes within  
894 the trajectory defined by the normalized pseudotime. **E)** Scatter plot showing the correlation  
895 between the distance to the tumor edge and the inferred pseudotime trajectory. Black dots  
896 represent the average normalized pseudotime for the set of Tcy located at a given distance  
897 from the tumor edge. The dashed red line represents the first-order derivative of the fitted  
898 curve. **F)** Histogram plots showing the average expression value of the markers used to define  
899 the pseudotime along the trajectory. The normalized distance to the tumor-edge (DTE) is also  
900 represented.  
901



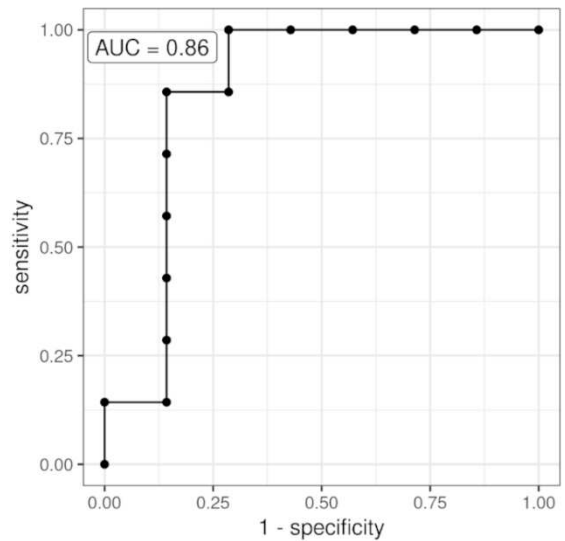
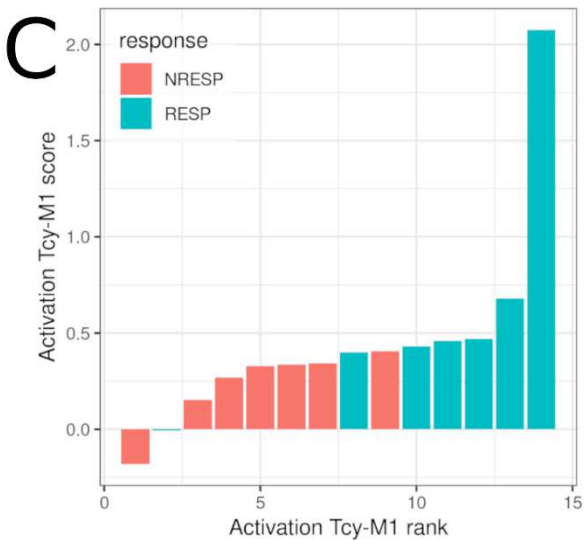
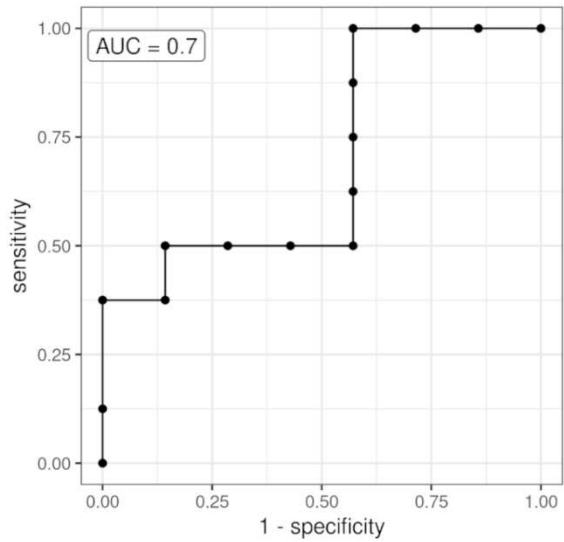
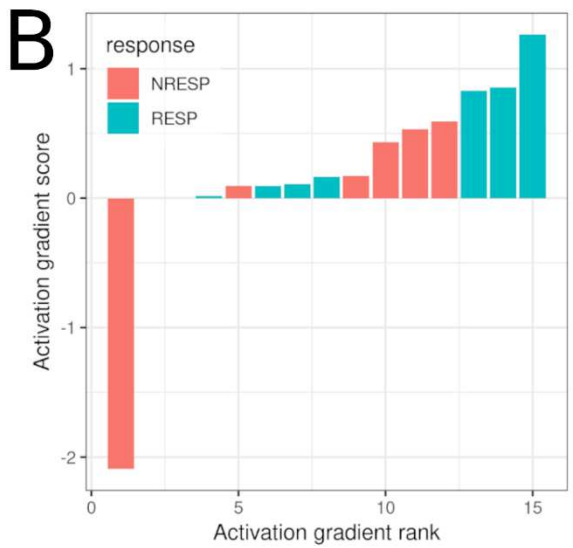
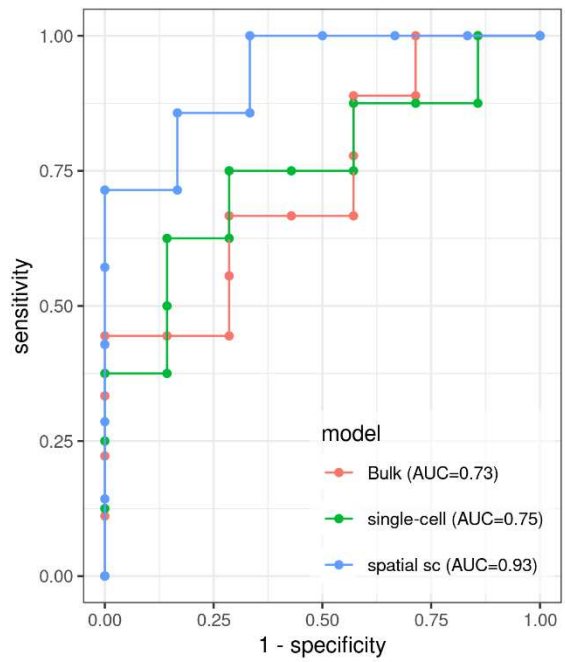
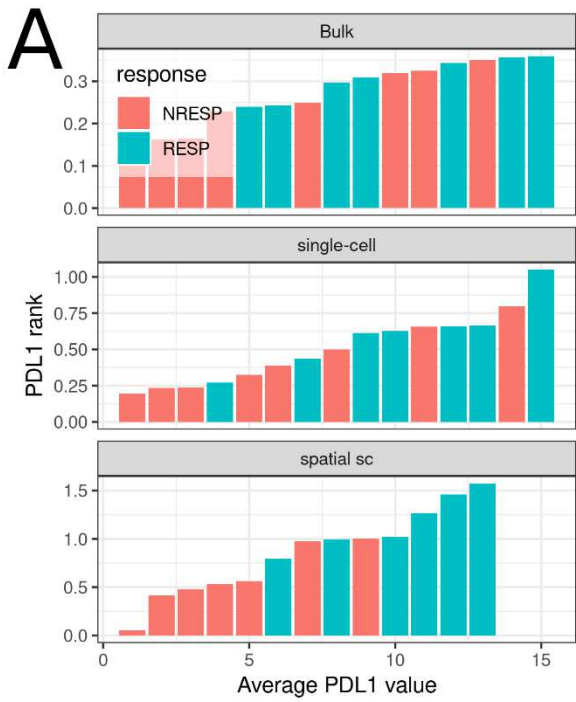
902  
903  
904  
905  
906  
907  
908  
909  
910  
911  
912  
913  
914  
915  
916  
917  
918  
919  
920  
921  
922  
923

**Figure 4 - PD-L1 expression in macrophages.** **A)** Boxplots showing PD-L1 expression in M1-like and M2-like macrophages in the different *in-silico* microdissected areas. (NTA: Non-tumor area, TSI: Tumor-stroma interface, TA: Tumor area), using pairwise t-test. **B)** PD-L1 gradient based on distance to the tumor edge. Green-shaded area represents the non-tumor area, gold-shaded area represents the TSI, red-shaded area represents the tumor-area. Dots represent the average PD-L1 expression in M1-like and M2-like macrophages at a certain distance of the tumor edge. Lines represent the fitted curves for those clouds of points. **C)** PD-L1 gradient based on distance to the tumor edge stratified by patient response. **D)** Boxplots showing PD-L1 expression based on discretized distance to closest Tcy (cut-off distance value: 100  $\mu\text{m}$ ) using pairwise t-test (fdr corrected). **E)** Scatter plot showing PD-L1 expression in M1-like and M2-like macrophages based on their distance to the closest Tcy. Each dot represents the average expression of the macrophages located at a certain distance from the closest Tcy (bins of 10  $\mu\text{m}$ ). Yellow-shaded area represents the 'close' region, light-blue-shaded area represents the 'far' region. **F)** Scatter plot showing the PD-L1 expression in M1-like and M2-like macrophages based on their distance to closest Tcy stratified by patient response (RESP: responders, NRESP: non-responders). **G)** Boxplots showing PD-L1 expression based on discretized distance to the edge and to closest Tcy using pairwise t-test (fdr corrected) (CC: Close-Close, CF: Close-Far, FC: Far-Close, FF: Far-Far). **H)** Boxplots showing PD-L1 expression based on discretized distance to the edge and to closest Tcy stratified by patient response using pairwise t-test (fdr corrected). ns: Not Significant, \* p value < 0.05, \*\* p value < 0.01.

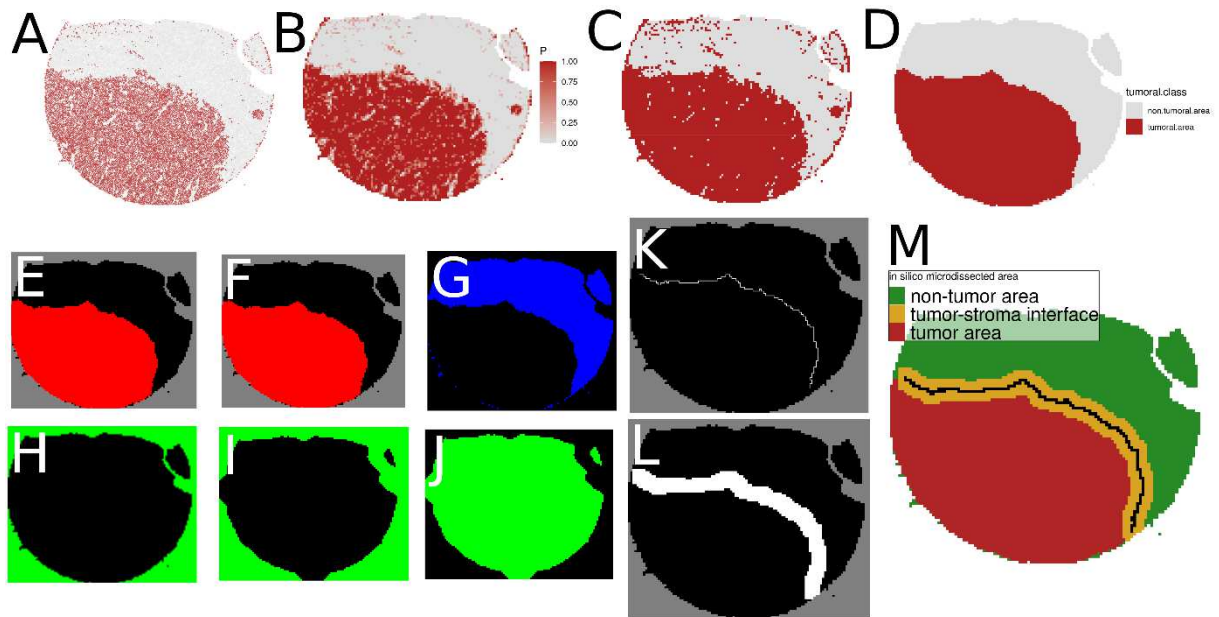


924  
925  
926  
927  
928  
929  
930  
931  
932  
933  
934  
935  
936  
937  
938

**Figure 5 - Tcy activation levels based on distance to closest macrophage.** **A)** Scatter plot showing average activation value of Tcy based on distance to closest macrophage. The Yellow-shaded area represents the 'close' region, the light-blue-shaded area represents the 'far' region. **B)** Scatter plot showing average activation value of Tcy based on distance to closest macrophage stratified by patient response. **C)** Boxplots showing the activation level of Tcy based on discretized distance to closest macrophage using pairwise t-test (fdr corrected). **D)** Boxplots showing the activation level of Tcy based on discretized distance to closest macrophage stratified by patient response using pairwise t-test (fdr corrected). **E)** Boxplots showing the activation level of Tcy based on discretized distance to closest macrophage and distance to the edge using pairwise t-test (fdr corrected) (CC: Close-Close, CF: Close-Far, FC: Far-Close, FF: Far-Far). **F)** Boxplots showing the activation level of Tcy based on discretized distance to closest macrophage and distance to the edge stratified by patient response using pairwise t-test (fdr corrected). ns: Not Significant, \* p value < 0.05, \*\* p value < 0.01, \*\*\* p value < 0.001.

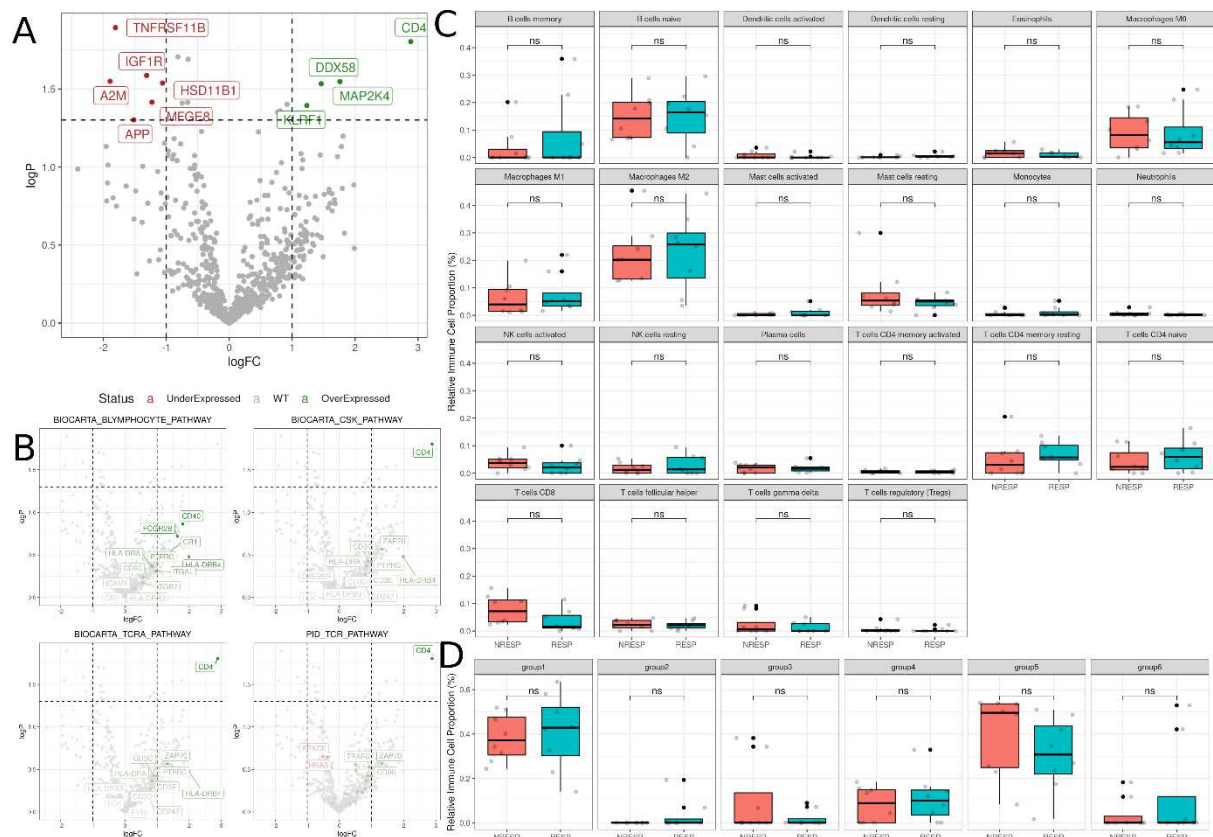


940 Figure 6 - High order biomarkers. **A)** Left: Barplots showing the average PD-L1 expression in  
941 all cells (top, 'Bulk'), M1-like macrophages (center, 'Single-cell'), and spatially selected  
942 (distance to tumor edge less than 30  $\mu\text{m}$  and distance to the closest Tcy less than 10  $\mu\text{m}$ ) M1-  
943 like macrophages (bottom, 'Spatial single-cell') for each patient and colored by patient  
944 response: responders (RESP), non-responders (NRESP). Right: ROC curves corresponding  
945 to the score rankings for the different candidate biomarkers. **B)** Left: Barplot showing the  
946 difference in Tcy activation between tumor and non-tumor areas for RESP and NRESP  
947 patients. Each bar represents a patient. The module of the bar is calculated as the difference  
948 between the average Tcy activation in the non-tumor area and the average Tcy activation in  
949 the tumor area. Activation values were first normalized (z-scores) for each core. Right: ROC  
950 curve corresponding to the score ranking. **C)** Left: Barplot showing the average Tcy activation  
951 level at less than 10  $\mu\text{m}$  from the closest M1-like macrophage. Right: ROC curve  
952 corresponding to the score ranking.  
953



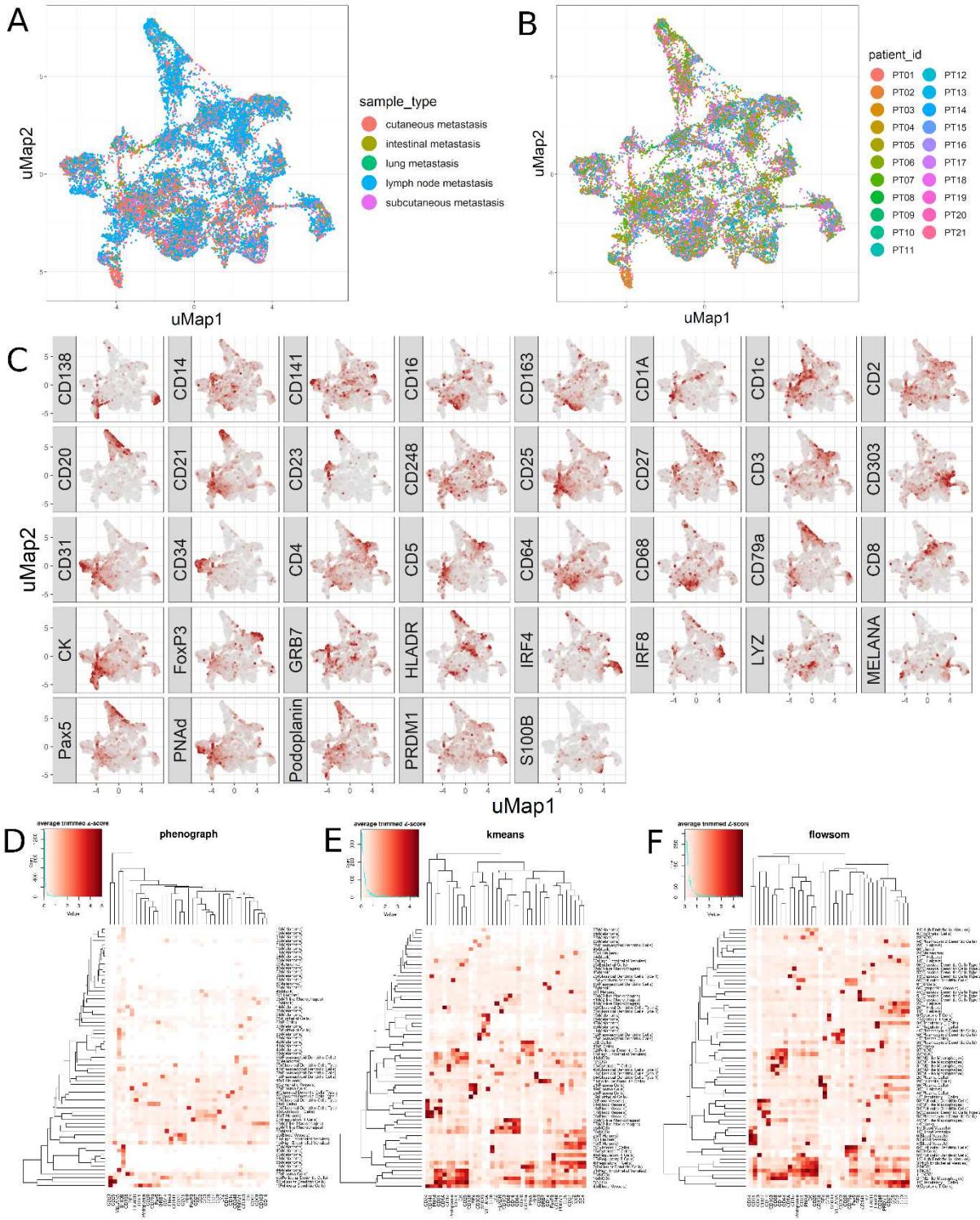
954  
 955  
 956  
 957  
 958  
 959  
 960  
 961  
 962  
 963  
 964  
 965  
 966  
 967  
 968  
 969  
 970  
 971  
 972

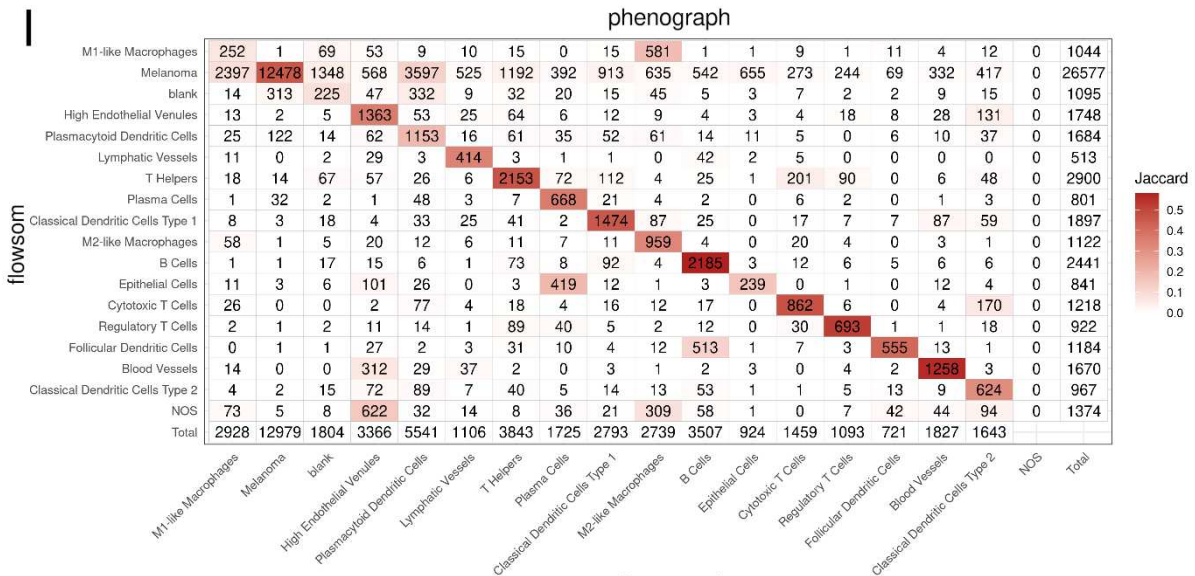
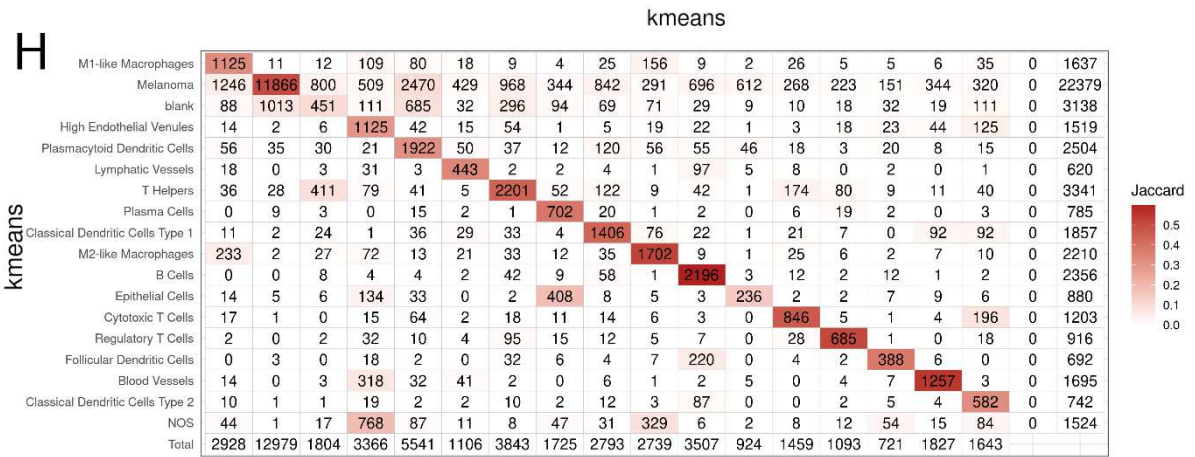
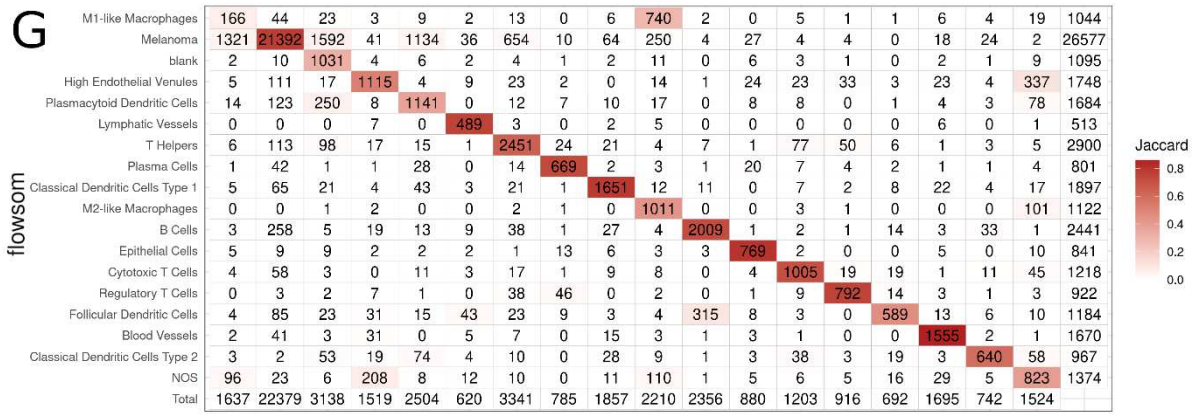
**Supplementary Figure 1 - In-silico microdissection.** **A)** Scatter plot of a representative core from sample MEL9 from patient PT7. Melanoma cells are colored in red. Any other cell phenotype is colored in grey. **B)** Heatmap representing the proportion (P) of melanoma cells after tiling the tissue in squares of 50x50px. **C)** Binary mask obtained after applying a cut-off of  $P > 0$  to B. **D)** Binary mask obtained after applying a median filter to C. Tumoral areas are shown in red, non-tumor areas are shown in grey. **E)** Tumor mask used to calculate the tumor edge. Red: tumor positive, Black: tumor negative, Grey: areas without tissue. **F)** Dilated tumor mask after applying a box kernel of 5px of diameter to F. **G)** Tumor negative mask (blue) after applying a dilation function with a box kernel of 51px of diameter to the 1-complement of F. **H)** Positive mask for areas without tissue (green). **I)** Outside mask after applying a dilation function with a box kernel of 251px of diameter to H. **J)** 1-complementary of I (tissue removing edges). **K)** Tumor edge: overlapping between the masks obtained in F (dilated tumor positive), G (dilated tumor negative), and J (tissue without edges). **L)** Tumor stroma interface: obtained mask after dilating the tumor edge with a box kernel of 301px of diameter. **M)** *In-silico* microdissected tissue: red represents the tumor area (E), green represents the non-tumor area, gold represents the tumor-stroma interface (L), the black line represents the tumor edge (K).



973  
 974  
 975  
 976  
 977  
 978  
 979  
 980  
 981  
 982  
 983  
 984  
 985  
 986  
 987  
 988

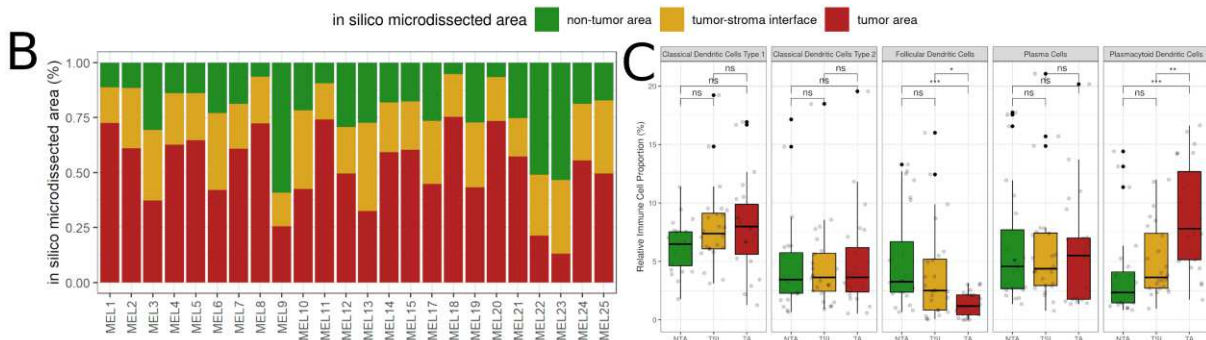
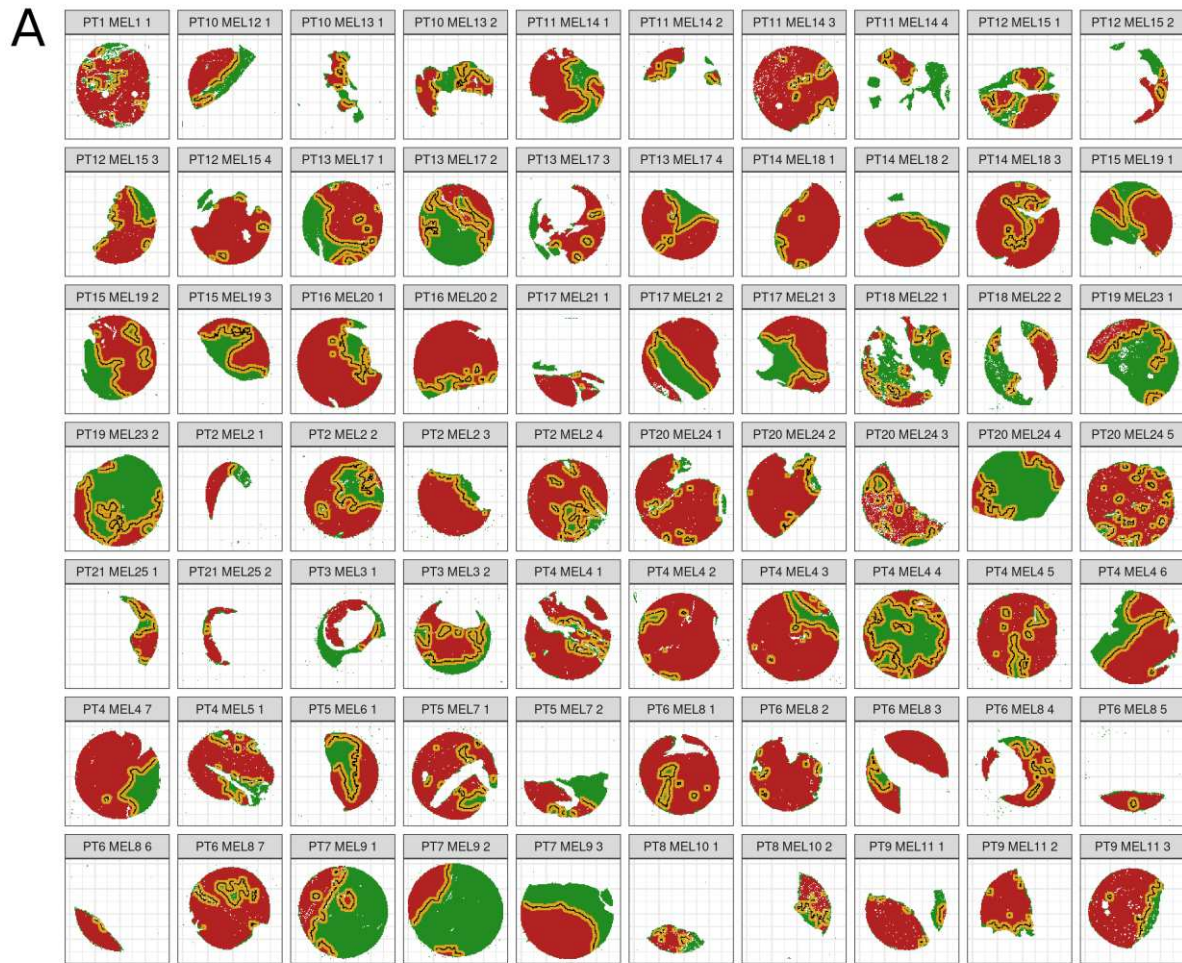
**Supplementary Figure 2 – Nanostring Analysis.** **A)** Volcano plot showing the results from differential gene expression analysis: genes colored in green represent genes overexpressed in responders (RESP) when compared to non-responders (NRESP); genes colored in red represent genes underexpressed in RESP when compared to NRESP; the rest of the genes are represented in gray. Dashed lines represent the thresholds used to define statistical significance ( $\logFC = -1/+1$ ,  $p\text{-value} = 0.05$ ). **B)** Volcano plot showing the results from gene-set enrichment analysis. Labelled genes represent genes belonging to the specific pathway, all the rest of genes are colored as gray dots. **C)** Digital cytometry analysis using CibersortX for general immune populations. The LM22 signature matrix was used. None of the included immune types show significant differences when comparing the fractions of RESP vs NRESP patients (Wilcoxon test). **D)** Digital cytometry analysis using CibersortX for Tcy subtypes. The signature matrix was generated using the data included in Sade-Feldman et al<sup>29</sup>. None of the included subtypes showed significant differences when comparing fractions from RESP and NRESP patients. NS: not significant.





990  
 991 **Supplementary Figure 3 - Phenotypic identification. A-B)** uMaps colored by the different sites  
 992 of biopsy (sample\_type) and patients (patient\_id) included in the analysis. **C)** uMap colored by  
 993 each of the 37 markers included in the phenotypic identification. Red dots represent cells with  
 994 high expression for the given marker. Grey dots represent cells with low/no expression for the  
 995 given marker. **D-F)** Heatmaps representing the fingerprint for each identified cluster and their  
 996 corresponding annotation for the PhenoGraph, KMeans, and FlowSom methods respectively.  
 997 Rows represent clusters, columns represent markers. The color in each tile represents the  
 998 average expression of the marker for a given cluster. Rows and columns are sorted by  
 999 hierarchical clustering. **G-I)** Jaccard matrices showing the stability between the different

1000 clustering methods: FlowSom vs KMeans, KMeans vs PhenoGraph, and FlowSom vs  
1001 PhenoGraph respectively. Rows and columns represent the identified cell phenotypes. The  
1002 value inside each cell in the matrix represents the number of cells annotated as such in the  
1003 two clustering methods. The color of each cell in the matrix represents the Jaccard distance  
1004 between the cell types in the specific row/column.  
1005



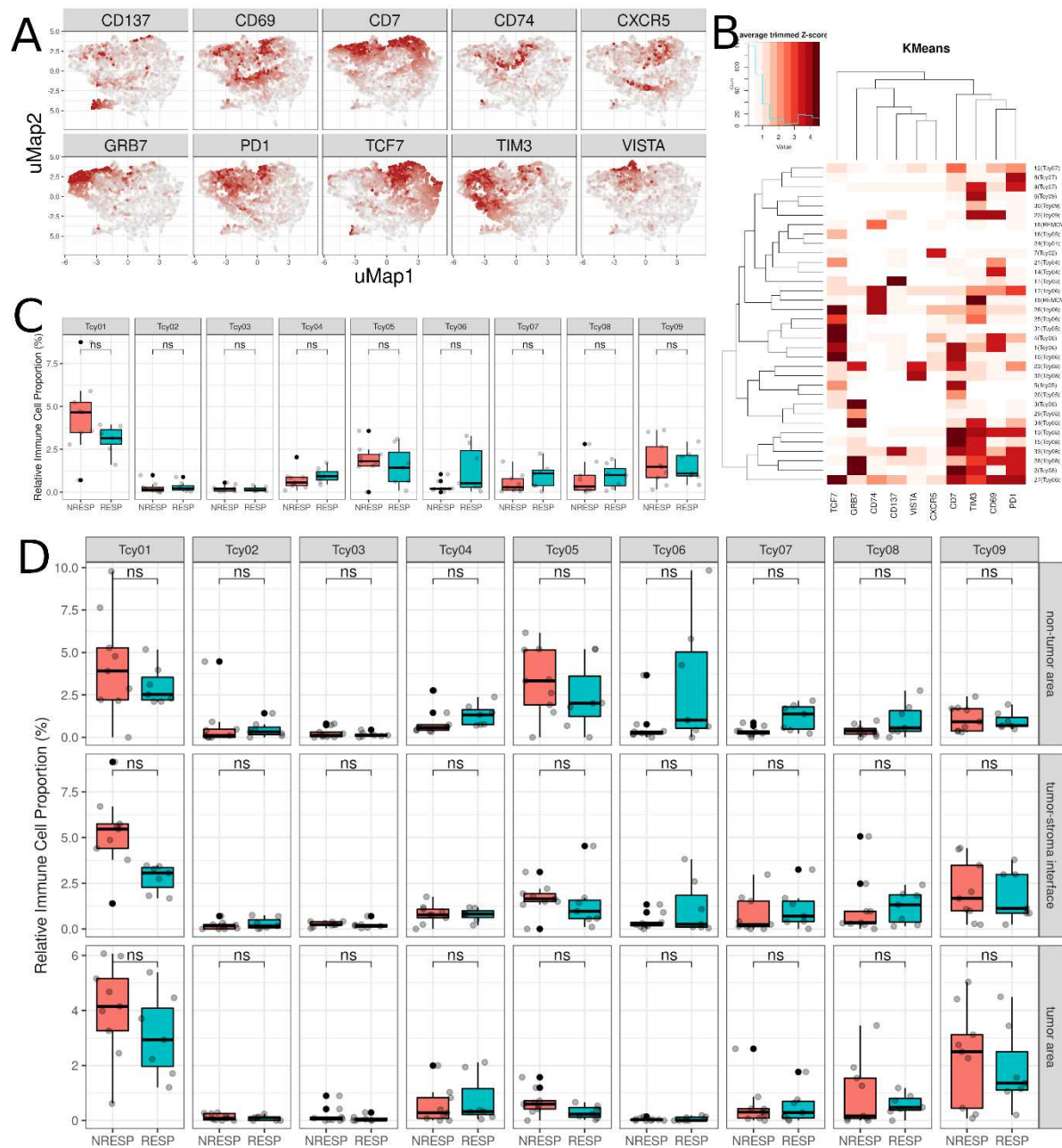
1006  
1007  
1008  
1009  
1010  
1011  
1012  
1013  
1014  
1015

**Supplementary Figure 4 - In-silico microdissection.** **A)** *In-silico* microdissection results for all the tissue cores included in the analysis with patient, sample and core ID. **B)** Stacked bar plots showing interpatient variability. Bars represent the relative area (%) covered by the different *in-silico* microdissected areas in each patient. **C)** Cell composition analysis of selected cell phenotypes comparing the relative proportion of immune cells in the different *in-silico* microdissected areas (NTA: Non-tumor area, TSI: Tumor-stroma interface, TA: Tumor area), using pairwise Wilcoxon test. ns: Not Significant, \* p value < 0.05, \*\* p value < 0.01, \*\*\* p value < 0.001.



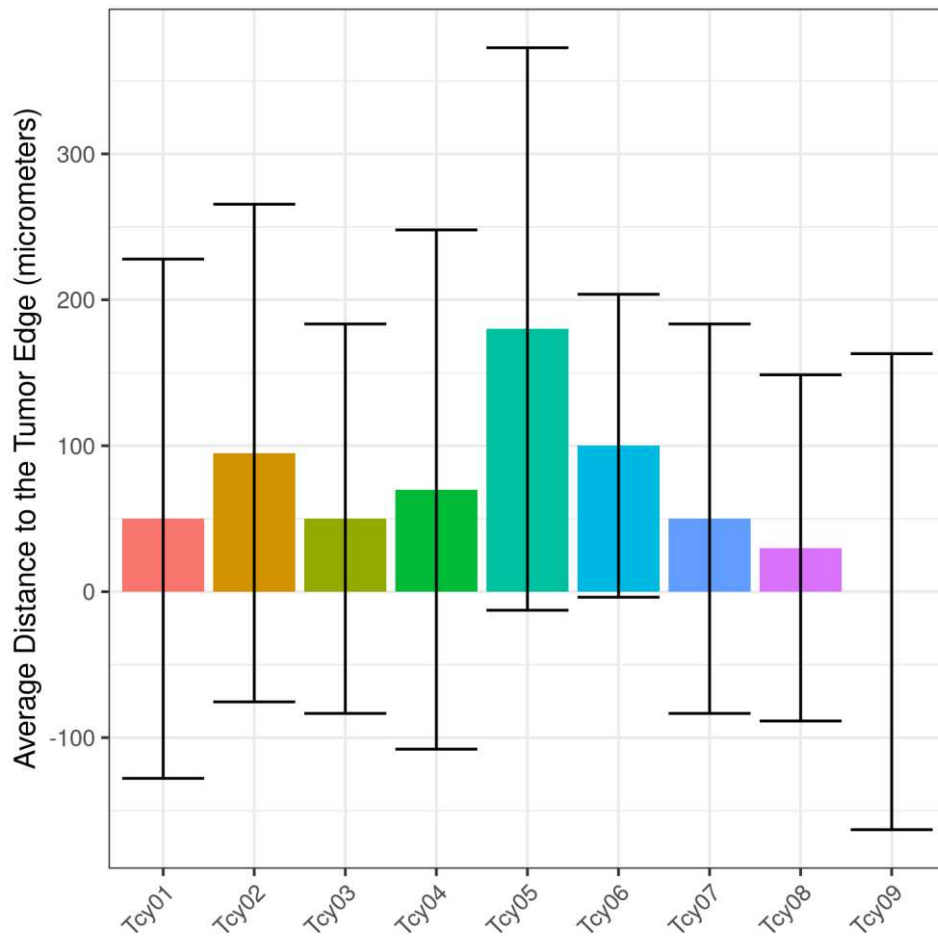
1016  
 1017  
 1018  
 1019  
 1020  
 1021

**Supplementary Figure 5: Response-related cytometry analysis. A) General cytometry.** Boxplots showing the relative immune cell proportion (%) of each identified cell phenotype comparing responding (RESP, n=7) vs non-responding (NRESP, n=8) patients (Wilcoxon test). **B) Cytometry analysis in the different *in-silico* microdissected areas.** NS: not significant.



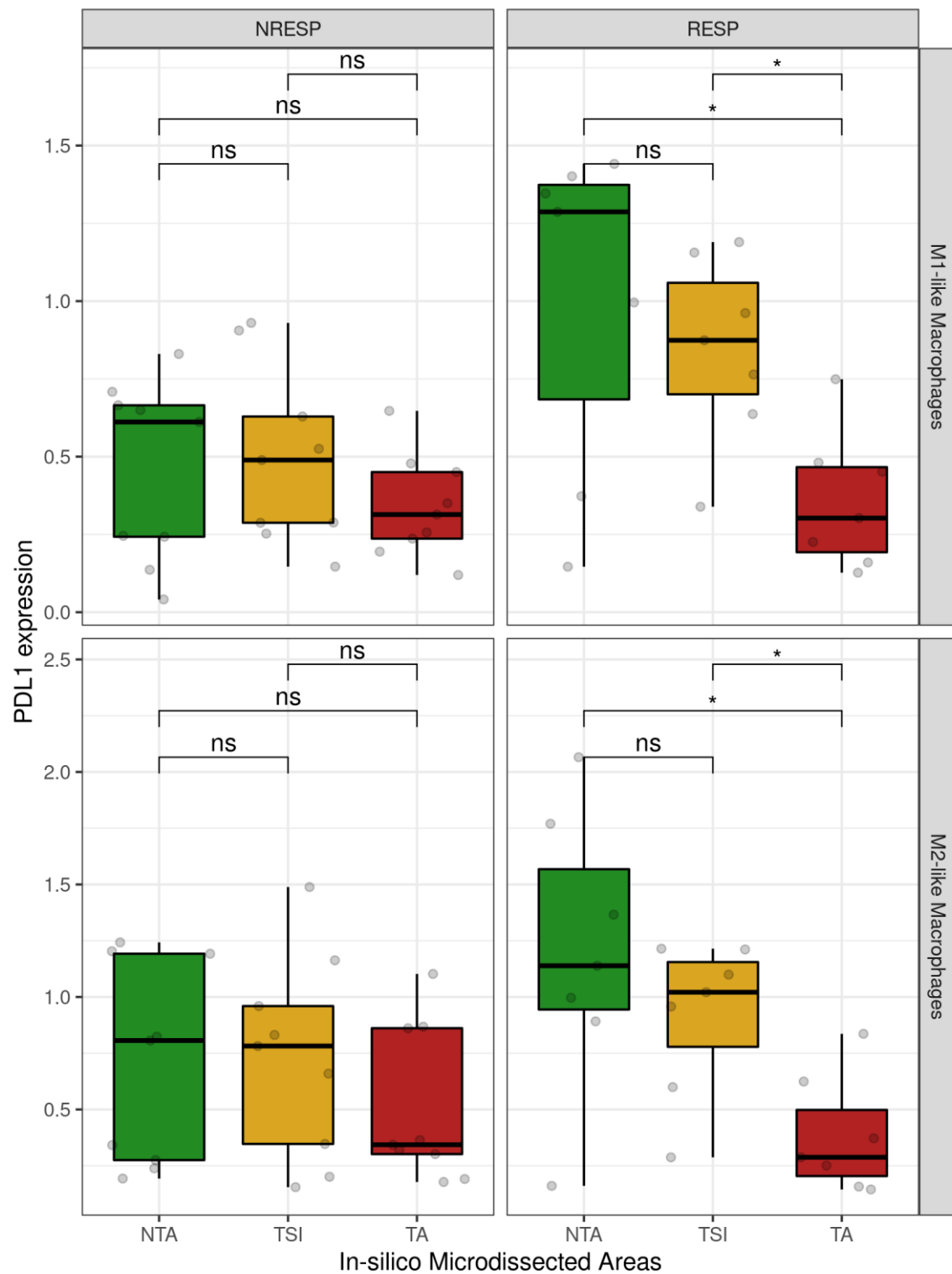
1022  
 1023  
 1024  
 1025  
 1026  
 1027  
 1028  
 1029  
 1030  
 1031  
 1032  
 1033

**Supplementary Figure 6 - Profiling of cytotoxic T-cells: cytometry.** **A**) uMap colored by each of the 10 markers included in the clustering. Red dots represent cells with high expression for the given marker. Grey dots represent cells with low/no expression for the given marker. **B**) Heatmap representing the fingerprint for each identified cluster and their corresponding annotation for the KMeans method. Rows represent clusters, columns represent markers. The color in each tile represents the average expression of the marker for a given cluster. Rows and columns are sorted by hierarchical clustering. **C**) General cytometry. Boxplots showing the relative Tcy proportion (%) of each identified subtype comparing responding (RESP, n=7) vs non-responding (NRESP, n=8) patients (Wilcoxon test). **D**) Cytometry analysis in the different *in-silico* microdissected areas. NS: not significant.



1034  
 1035  
 1036  
 1037  
 1038

*Supplementary Figure 7 - Tcy profiling: distance to the tumor edge.* Barplots indicating the average distance (in micrometers) from the different identified Tcy subtypes to the tumor edge. The black line indicates the standard deviation of each distribution.



1039  
 1040  
 1041  
 1042  
 1043  
 1044

Supplementary Figure 8 - Spatial effect on macrophage PD-L1 expression. Boxplots showing PD-L1 expression in M1-like and M2-like macrophages for the different *in-silico* microdissected areas separately for responding (RESP) and non-responding (NRESP) patients. Significance was calculated using pairwise Wilcoxon test (fdr corrected). ns: Not Significant, \* p value < 0.05.

## Supplementary Files

This is a list of supplementary files associated with this preprint. Click to download.

- [SupplementaryTable1Overviewclinicalsamplesincludedforanalysis.docx](#)
- [SupplementaryTable2OverviewantibodiesusedforMILAN.docx](#)
- [SupplementaryTable3Cellcomposition.docx](#)
- [SupplementaryTable4GLSNanostring.xlsx](#)
- [SupplementaryTable5GSANanostring.xlsx](#)